#### **OPEN ACCESS**



# Cosmological-scale Ly $\alpha$ Forest Absorption around Galaxies and AGNs Probed with the HETDEX and SDSS Spectroscopic Data

Dongsheng Sun<sup>1,2</sup>, Ken Mawatari<sup>1,3</sup>, Masami Ouchi<sup>3,1,4,5</sup>, Yoshiaki Ono<sup>1</sup>, Hidenobu Yajima<sup>6</sup>, Yechi Zhang<sup>1,2,4</sup>, Makito Abe<sup>6</sup>, William P. Bowman<sup>7</sup>, Erin Mentuch Cooper<sup>8,9</sup>, Dustin Davis<sup>8</sup>, Daniel J. Farrow<sup>10,11</sup>, Karl Gebhardt<sup>8</sup>, Gary J. Hill<sup>8,9</sup>, Chenxu Liu<sup>8,12</sup>, and Donald P. Schneider<sup>13,14</sup> <sup>1</sup> Institute for Cosmic Ray Research, The University of Tokyo, 5-1-5 Kashiwanoha, Kashiwa, Chiba 277-8582, Japan; sunds@icrr.u-tokyo.ac.jp

<sup>2</sup> Department of Astronomy, Graduate School of Science, the University of Tokyo, 7-3-1 Hongo, Bunkyo, Tokyo 113-0033, Japan National Astronomical Observatory of Japan, 2-21-1 Osawa, Mitaka, Tokyo 181-8588, Japan <sup>4</sup> Kavli Institute for the Physics and Mathematics of the Universe (Kavli IPMU, WPI), The University of Tokyo, 5-1-5 Kashiwanoha, Kashiwa, Chiba, 277-8583, Japan <sup>5</sup> Department of Astronomical Science, SOKENDAI (The Graduate University for Advanced Studies), 2-21-1 Osawa, Mitaka, Tokyo, 181-8588, Japan Center for Computational Sciences, University of Tsukuba, Ten-nodai, 1-1-1 Tsukuba, Ibaraki 305-8577, Japan Department of Astronomy, The University of Texas at Austin, 2515 Speedway Boulevard, Austin, TX 78712, USA

M. Donald Observation Transfer of Astronomy and Transfer of Texas at Austin, 2515 Speedway Boulevard, Austin, TX 78712, USA McDonald Observatory, The University of Texas at Austin, 2515 Speedway Boulevard, Austin, TX 78712, USA <sup>10</sup> University Observatory, Fakultät für Physik, Ludwig-Maximilians University Munich, Scheinerstrasse 1, D-81679 Munich, Germany Max-Planck Institut für extraterrestrische Physik, Giessenbachstrasse 1, D-85748 Garching, Germany <sup>12</sup> South-Western Institute for Astronomy Research, Yunnan University, Kunming, Yunnan, 650500, People's Republic of China Department of Astronomy & Astrophysics, The Pennsylvania State University, University Park, PA 16802, USA <sup>14</sup> Institute for Gravitation and the Cosmos, The Pennsylvania State University, University Park, PA 16802, USA Received 2023 January 8; revised 2023 March 22; accepted 2023 April 20; published 2023 June 29

#### **Abstract**

We present cosmological-scale three-dimensional neutral hydrogen (H I) tomographic maps at z=2-3 over a total of 837 deg<sup>2</sup> in two blank fields that are developed with Ly $\alpha$  forest absorptions of 14,736 background Sloan Digital Sky Survey (SDSS) quasars at z=2.08-3.67. Using the tomographic maps, we investigate the large-scale ( $\gtrsim 10~h^{-1}$  cMpc) average H I radial profiles and two-direction profiles of the line-of-sight (LOS) and transverse directions around galaxies and active galactic nuclei (AGNs) at z=2-3 identified by the Hobby–Eberly Telescope Dark Energy eXperiment survey and SDSS, respectively. The peak of the H I radial profile around galaxies is lower than the one around AGNs, suggesting that the dark matter halos of galaxies are less massive on average than those of AGNs. The LOS profile of AGNs is narrower than the transverse profile, indicating the Kaiser effect. There exist weak absorption outskirts at  $\gtrsim 30~h^{-1}$  cMpc beyond H I structures of galaxies and AGNs found in the LOS profiles that can be explained by the H I gas at  $\gtrsim 30~h^{-1}$  cMpc falling toward the source position. Our findings indicate that the H I radial profile of AGNs has transitions from proximity zones ( $\lesssim$ a few  $h^{-1}$  cMpc) to the H I structures ( $\sim 1-30~h^{-1}$  cMpc) and the weak absorption outskirts ( $\gtrsim 30~h^{-1}$  cMpc). Although there is no significant dependence of AGN types (type 1 vs. type 2) on the H I profiles, the peaks of the radial profiles anticorrelate with AGN luminosities, suggesting that AGNs' ionization effects are stronger than the gas mass differences.

*Unified Astronomy Thesaurus concepts*: Galaxies (573); Galaxy evolution (594); High-redshift galaxies (734); Intergalactic medium (813)

#### 1. Introduction

Galaxy formation in the universe is closely related to the neutral hydrogen (H I) gas in the intergalactic medium (IGM). Within the modern paradigm of galaxy formation, galaxies form and evolve in the filament structure of H I gas (e.g., Meiksin 2009; Mo et al. 2010). Cosmological hydrodynamics simulations suggest that the picture of galaxy formation and evolution is associated with large-scale baryonic gas exchange between the galaxy and the IGM (Fox 2017; van de Voort 2017).

The circulation of gas is one of the keys to understanding galaxy formation and evolution. The interplay of gravitational and feedback-driven processes can have surprisingly large effects on the large-scale behavior of the IGM. Some of the radiation produced by massive stars and black hole accretion

Original content from this work may be used under the terms of the Creative Commons Attribution 4.0 licence. Any further distribution of this work must maintain attribution to the author(s) and the title of the work, journal citation and DOI.

disks can escape from the dense gaseous environments and propagate out of galaxies and photoionize the H<sub>I</sub> gas in the circumgalactic medium (CGM) and even in the IGM (Mukae et al. 2020; National Academies of Sciences, Engineering, and Medicine 2021).

Great progress has been achieved in exploring the  $Ly\alpha$  forest absorption around galaxies and active galactic nuclei (AGNs). The cross-correlation of the H I in the IGM and galaxies has been detected by  $Ly\alpha$  absorption features in the spectra of background quasars (e.g., Rauch 1998; Faucher-Giguère et al. 2008a; Prochaska et al. 2013) and bright star-forming galaxies (Steidel et al. 2010; Mawatari et al. 2016; Thomas et al. 2017). The Keck Baryon Structure Survey (KBSS; Rakic et al. 2012; Rudie et al. 2012; Turner et al. 2014), the Very Large Telescope LBG Redshift Survey (VLRS; Crighton et al. 2011; Tummuangpak et al. 2014), and other spectroscopic programs (e.g., Adelberger et al. 2003, 2005) have investigated the detailed properties of the  $Ly\alpha$  forest absorption around galaxies. These observations target H I gas around galaxies on the scale of the CGM. Recently, three-dimensional (3D) H I

tomography mapping, a powerful technique to reconstruct the large-scale structure of HI gas, has been developed by Lee et al. (2014, 2016, 2018). HI tomography mapping was originally proposed by Pichon et al. (2001) and Caucci et al. (2008) with the aim of reconstructing the 3D matter distribution from the Ly $\alpha$  transmission fluctuation of multiple sight lines. By this technique, the COSMOS Ly $\alpha$  Mapping and Tomo-Observations (CLAMATO) graphy survev et al. 2014, 2018) has revealed H I large-scale structures with spatial resolutions of  $2.5 \ h^{-1}$  comoving megaparsecs (cMpc). This survey demonstrates the power of 3D H I tomography mapping in a number of applications, including the study of a protocluster at z = 2.44 (Lee et al. 2016) and the identification of cosmic voids (Krolewski et al. 2018). Due to an interpolation algorithm (Section 4.3) used in the reconstruction of the 3D H I tomography map, we are able to estimate the Ly $\alpha$ forest absorption along lines of sight (LOSs) where there are no available background sources. Based on the 3D H I tomography map of the CLAMATO survey, Momose et al. (2021) have reported measurements of the IGM H Igalaxy cross-correlation function (CCF) for several galaxy populations. Due to the limited volume of the CLAMATO 3D IGM tomography data, Momose et al. (2021) cannot construct the CCFs at scales over  $24 h^{-1}$  cMpc in the direction of transverse to the LOS. Mukae et al. (2020) have investigated a larger field than the one of Momose et al. (2021) using 3D H I tomography mapping and report a huge ionized structure of HI gas associated with an extreme QSO overdensity region in the EGS field. Mukae et al. (2020) interpret the large ionized structure as the overlap of multiple proximity zones that are photoionized regions created by the enhanced ultraviolet background (UVB) of quasars. However, Mukae et al. (2020) found only one example of a huge ionized bubble, and no others have been reported in the literature.

Despite the great effort made by previous studies, the limited volume of previous work prevents us from understanding how ubiquitous or rare these large ionized structures are. In order to answer this question, we must investigate the statistical Ly $\alpha$  forest absorptions around galaxies and AGNs at much larger spatial scales ( $\gtrsim 10\,h^{-1}$  cMpc). Although Momose et al. (2021) derived CCFs for different populations—Ly $\alpha$  emitters (LAEs), H $\alpha$  emitters (HAEs), [O III] emitters (O3Es), AGNs, and submillimeter galaxies (SMGs)—on a scale of more than  $20~h^{-1}$  cMpc, the limited sample size results in large uncertainties in the CCF at large scales and prevents definitive conclusions from being made regarding the statistical Ly $\alpha$  forest absorptions around galaxies and AGNs.

Another open question is the luminosity and AGN type dependence of the large-scale Ly $\alpha$  forest absorption around AGNs. Font-Ribera et al. (2013) have estimated the Ly $\alpha$  forest absorption around AGNs using the Sloan Digital Sky Survey (SDSS; York et al. 2000) data release 9 quasar catalog (DR9Q; Pâris et al. 2011) and find no dependence of the Ly $\alpha$  forest absorption on AGN luminosity. In this study, we investigate the luminosity dependence using the SDSS data release 14 quasar (DR14Q; Pâris et al. 2018) catalog, which includes sources  $\sim$ 2 mag fainter than those used by Font-Ribera et al. (2013). In the AGN unification model (Antonucci & Miller 1985; see also Spinoglio & Fernández-Ontiveros 2021), which provides a physical picture that a hot accretion disk of a supermassive black hole is obscured by a dusty torus, the type 1 and type 2 classes are produced by different accretion disk

viewing angles. In this picture, the type 1 (type 2) AGN is biased to AGNs with a wide (narrow) opening angle. In the case of type 1 AGNs, one can directly observe the accretion disks and the broad-line region, while for type 2 AGNs, only the narrow-line region is observable. Previous studies have identified the proximity effect that the IGM of type 1 AGN is statistically more ionized owing to the local enhancement of the UV background on the LOS passing near the AGN (Faucher-Giguère et al. 2008b). Based on the unification model, the type 2 AGN obscured on the LOS statistically radiates in the transverse direction. The investigation of the AGN type dependence on the surrounding H I can reveal the large-scale Ly $\alpha$  forest absorption influenced by the direction of radiation from the AGN.

To investigate the Ly $\alpha$  forest absorptions around galaxies and AGNs on large scales, over tens of  $h^{-1}$  cMpc, we need to conduct a new study in a field with length of any side larger than 100  $h^{-1}$  cMpc. We reconstruct 3D H I tomography maps of Ly $\alpha$  forest absorption at  $z\sim2$ –3 in a total area of 837 deg<sup>2</sup>. We use  $\gtrsim$ 15,000 background sight lines from SDSS quasars (Pâris et al. 2018; Lyke et al. 2020) for the H I tomography map reconstruction and have a large number of unbiased galaxies and AGNs from the Hobby–Eberly Telescope Dark Energy eXperiment (HETDEX; Gebhardt et al. 2021) survey and SDSS for the investigations of the large-scale Ly $\alpha$  forest absorptions around galaxies and AGNs.

This paper is organized as follows. Section 2 describes the details of the HETDEX survey and our spectroscopic data. Our foreground and background samples of galaxies and AGNs are presented in Section 3. The technique of creating the HI tomography mapping and the reconstructed HI tomography map are described in Section 4, and the observational results of Ly $\alpha$  forest absorptions around galaxies and AGNs are given in Section 5. In this section, we also interpret our results in the context of previous studies and investigate the dependence of our tomography maps on AGN type and luminosity. We adopt a cosmological parameter set of  $(\Omega_m, \Omega_\Lambda, h) = (0.29, 0.71, 0.7)$  in this study.

#### 2. Data

#### 2.1. HETDEX Spectra

HETDEX provides an untargeted, wide-area, integral field spectroscopic survey and aims to determine the evolution of dark energy in the redshift range 1.88-3.52 using  $\sim 1$  million LAEs over  $540~\rm deg^2$  in the northern and equatorial fields, which are referred to as "Spring" and "Fall" fields, respectively. The total survey volume is  $\sim 10.9$  comoving Gpc<sup>3</sup>.

The HETDEX spectroscopic data are gathered using the 10 m Hobby–Eberly Telescope (HET; Ramsey et al. 1994; Hill et al. 2021) to collect light for the Visible Integral-field Replicable Unit Spectrograph (VIRUS; Hill et al. 2018, 2021) with 78 integral field unit (IFU; Kelz et al. 2014) fiber arrays. VIRUS covers a wavelength with resolving power ranging from 750 to 950. Each IFU has 448 fibers with a 1.75 diameter. The 78 IFUs are spread over the 22′ field of view, with a 1/4.6 fill factor. Here we make use of data release 2 of the HETDEX (HDR2; Cooper et al. 2023) over the Fall and Spring fields. In this study, we investigate the fields where HETDEX survey data are taken between 2017 January and 2020 June. The effective area is  $11,542 \text{ arcmin}^2$ . The estimated depth of an emission line at  $S/N = 5 \text{ reaches } (3-4) \times 10^{-17} \text{ erg cm}^{-2} \text{ s}^{-1}$ .

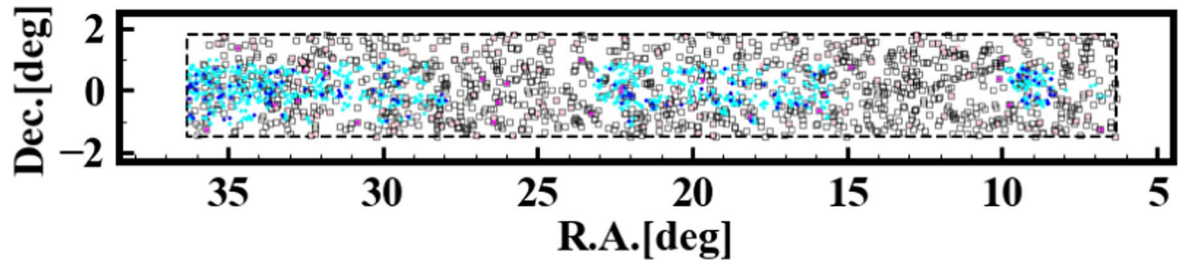


Figure 1. Sky distribution of the foreground AGNs and galaxies at z = 2.0–2.2 in the ExFall field. The squares present the positions of All-AGN sample sources. Pink (magenta) squares represent the sources of the T1-AGN (T2-AGN) sample. The cyan and blue circles show the positions of the galaxy and T1-AGN(H) sample sources, respectively. The black dashed line indicates the border of the H I tomography map in the Exfall field.

#### 2.2. Subaru HSC Imaging

The HETDEX-HSC imaging survey was carried out in a total time allocation of three nights in 2015–2018 (semesters S15A, S17A, and S18A; PI: A. Schulze) and 2019–2020 (semester S19B; PI: S. Mukae) over a ~250  $\deg^2$  area in the Spring field, accomplishing a  $5\sigma$  limiting magnitude of  $r\!=\!25.1$  mag. The SSP-HSC program has obtained deep multicolor imaging data on the 300  $\deg^2$  sky, half of which overlaps with the HETDEX footprints. In this study, we use the r-band imaging data from public data release 2 (PDR2) of SSP-HSC. The  $5\sigma$  depth of the SSP-HSC PDR2 r-band imaging data is typically 27.7 mag for the 3"0 diameter aperture. The data reduction of the HETDEX-HSC survey and SSP-HSC program is processed with HSC pipeline software hscPipe (Bosch et al. 2018) version 6.7.

Because the spectral coverage width of the HETDEX survey is narrow, only 2000 Å, most sources appear as single-line emitters. Furthermore, since the O II doublet is not resolved, we rely on the equivalent width (EW) to distinguish Ly $\alpha$  from O II. The high-z Ly $\alpha$  emission is typically stronger than low-z [O II] lines, due to the intrinsic line strengths and the cosmological effects. The continuum estimate from the HETDEX spectra reaches about g=25.5 (Davis et al. 2021; Cooper et al. 2023), and we improve on this using the deep HSC imaging. We estimate EW using continua measured from two sets of images taken by the HSC r-band imaging survey for HETDEX (HETDEX-HSC survey) and the Subaru Strategic Program (SSP-HSC; Aihara et al. 2018). Davis et al. and Cooper et al. find our contamination of O II emitters in the LAE sample to be below 2%.

# 2.3. SDSS-IV eBOSS Spectra

We use quasar data from eBOSS (Dawson et al. 2016), which is publicly available in the SDSS Data Release 14 and 16 quasar catalogs (DR14Q, DR16Q; Pâris et al. 2018; Lyke et al. 2020). The cosmology survey, eBOSS, is part of SDSS-IV. The eBOSS quasar targets are selected by the XDQSOz method (Bovy et al. 2012) and the color cut

$$m_{\text{opt}} - m_{\text{WISE}} \geqslant (g - i) + 3,$$
 (1)

where  $m_{\rm opt}$  is a weighted stacked magnitude in the g, r, and i bands and  $m_{\rm WISE}$  is a weighted stacked magnitude in the W1 and W2 bands of the Wide-field Infrared Survey Explorer (WISE; Wright et al. 2010). The aim of eBOSS is to accomplish precision angular diameter distance measurements and the Hubble parameter determination at  $z \sim 0.6$ –3.5 using different tracers of the underlying density fields over 7500 deg<sup>2</sup>. Its final goal is to obtain spectra of  $\sim$ 2.5 million luminous red galaxies,  $\sim$ 1.95 million emission-line galaxies,  $\sim$ 450,000 QSOs at  $0.9 \le z \le 2.2$ ,

and the Ly $\alpha$  forest of 60,000 QSOs at z > 2 over 4 yr of operation.

The eBOSS program is conducted with twin SDSS spectrographs (Smee et al. 2013), which are fed by 1000 fibers connected from the focal plane of the 2.5 m Sloan telescope (Gunn et al. 2006) at Apache Point Observatory. SDSS spectrographs have a fixed spectral bandpass of 3600–10000 Å over the 7 deg<sup>2</sup> field of view. The spectral resolution varies from 1300 at the blue end to 2600 at the red end, where 1 pixel corresponds to 1.8–5.2 Å.

### 3. Samples

Our study aims to map the statistical distribution of H I gas on a cosmological scale around foreground galaxies and AGNs by the 3D H I tomography mapping technique with background sources at z = 2-3. We use the foreground galaxies, foreground AGNs, and background sources presented in Sections 3.1, 3.2, and 3.3, respectively.

Two of the goals of this study are to explore the dependence of luminosity and AGN type on the Ly $\alpha$  forest absorption. To examine statistical results, we need a large number of bright AGNs and type 2 AGNs. Compared to moderately bright AGNs and type 1 AGNs, bright AGNs and type 2 AGNs are relatively rare. To obtain a sufficiently large samples of bright AGNs and type 2 AGNs, we expand the Spring and Fall fields of the HETDEX survey, from which we are able to investigate the statistical luminosity and AGN type dependence of the HI distribution around AGNs (Section 3.2). The northern extended Spring field flanking the HETDEX survey fields, referred to as the "ExSpring field," covers over 738 deg<sup>2</sup>, while the equatorial extended Fall field flanking the HETDEX survey fields, hereafter "ExFall field," covers 99 deg<sup>2</sup>. The total area of our 3D H I tomography mapping field is 837 deg<sup>2</sup> in the ExSpring and ExFall fields, which is referred to as "our study field." Our analysis is conducted in our study field where the foreground galaxies+AGNs and the background sources overlap on the sky. As an example, we present the foreground galaxies+AGNs in the ExFall field at z = 2.0-2.2 in Figure 1. The remaining foreground galaxies and AGNs investigated in this study are displayed in Figure 27, 28, and 29 of the Appendix. We also present the sky distribution of the background sources within the ExFall field in Figure 2. The rest of the background sources are shown in Figure 30 of the Appendix.

# 3.1. Foreground Galaxy Sample

We make a sample of foreground galaxies from the data of the HETDEX spectra (Section 2.1) and the Subaru HSC images (Section 2.2). With these data, Zhang et al. (2021) have built a

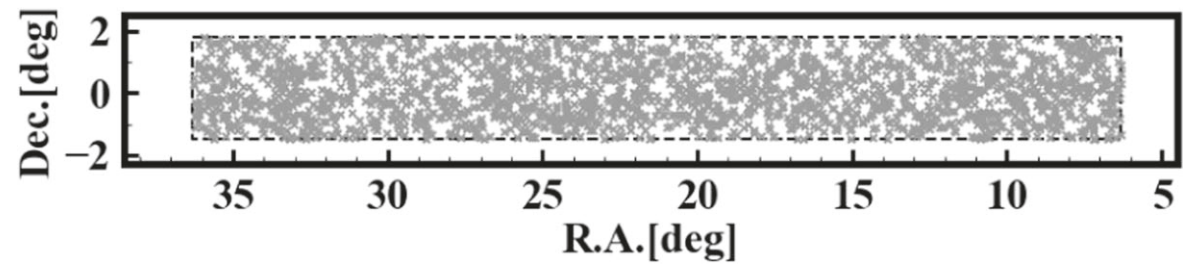


Figure 2. Sky distribution of background AGNs in the ExFall field. The gray crosses indicate background AGNs that are used to reconstruct our H I tomography map. The back dashed line has the same meaning as that in Figure 1.

Name of Sample	ExFall	ExSpring	Total	Survey	Criteria
Galaxy	3431	11,436	14,867	HETDEX	$EW_0 > 20 \text{ Å, FWHM}_{Ly\alpha} < 1000 \text{ km s}^{-1}, M_{UV} > -22 \text{ mag}$
T1-AGN(H)	438	1349	1787	HETDEX	${\rm EW}_0 > 20 \ {\rm \AA, FWHM_{Lylpha}} > 1000 \ {\rm km \ s^{-1}}$
T1-AGN	2393	12,300	14,693	SDSS	$FWHM_{Ly\alpha} > 1000 \text{ km s}^{-1}$
T2-AGN	436	1633	2069	SDSS	$\mathrm{FWHM}_{\mathrm{Ly}lpha} < 1000 \; \mathrm{km} \; \mathrm{s}^{-1}$

catalog of LAEs that have rest-frame EWs (EW0) of  $EW_0 > 20 \text{ Å}$  and HETDEX Emission Line eXplorer (ELiXer) probabilities (Davis et al. 2021, 2023) larger than 1. This EW<sub>0</sub> cut is similar to previous LAE studies (e.g., Gronwall et al. 2007; Konno et al. 2016). This catalog of LAEs is composed of 15,959 objects. Because the LAE catalog of Zhang et al. (2021) consists of galaxies, type 1 AGNs, and type 2 AGNs, we isolate galaxies from the sources of the LAE catalog with the limited observational quantities, Ly $\alpha$  and UV magnitude ( $M_{\rm UV}$ ), that can be obtained from the HETDEX and Subaru/HSC data. Because type 1 AGNs have broad-line Ly $\alpha$  emission, we remove sources with broad-line Ly $\alpha$  whose FWHM of the Ly $\alpha$  emission lines are greater than 1000 km s<sup>-</sup> To remove clear type 2 AGNs from the LAE catalog, we apply a UV magnitude cut of  $M_{\rm UV} > -22$  mag, which is the bright end of the UV luminosity function dominated by star-forming galaxies (Zhang et al. 2021). We then select sources in our study field and apply the redshift cut of z = 2.0-3.0 (as measured by the principle component analysis (PCA) of multiple lines; Pâris et al. 2018) to match the redshift range over which we construct the H I tomography map. These redshifts are measured with Ly $\alpha$ emission (Zhang et al. 2021) because Ly $\alpha$  is the only emission available for all of the sources.

By these selections, we obtain 14,130 star-forming galaxies from the LAE catalog. These 14,130 star-forming galaxies are referred to as the "galaxy" sample in this study.

#### 3.2. Foreground AGN Samples

In this subsection, we describe how we select foreground AGNs from two sources, (a) the combination of the HETDEX spectra and the HSC imaging data and (b) the SDSS DR14Q catalog. The type 1 AGNs are identified with sources (a) and (b), while the type 2 AGNs are drawn from source (b).

With source (a) being the same as the one stated in Section 3.1, Zhang et al. (2021) have constructed the LAE catalog. We use the catalog of Zhang et al. (2021) to select LAEs at  $z \sim 2-3$  that fall in our study field. Applying a Ly $\alpha$  line width criterion of FWHM > 1000 km s<sup>-1</sup> with the HETDEX spectra, we identify broad-line AGNs, i.e., type 1 AGNs, from the LAEs. We thus obtain 1829 type 1 AGNs that are referred to as T1-AGN(H).

We use the width of the Ly $\alpha$  emission line for the selection of type 1 AGNs. This is because no other emission lines characterizing AGNs, e.g., C IV, are available for all of the LAEs owing to the limited wavelength coverage and the sensitivity of HETDEX. Similarly, the redshifts of T1-AGN(H) objects are measured with Ly $\alpha$  emission whose redshifts may be shifted from the systemic redshifts by up to a few hundred kilometers per second (See Section 3.1). We do not select type 2 AGNs from source (a) because we cannot identify type 2 AGNs easily with the given data set of source (a).

From source (b), we obtain the other samples of foreground AGNs. We first choose objects with a classification of QSOs of the SDSS DR14Q and remove objects outside the redshift range of z=2.0–3.0 in our study field. We obtain 23,721 AGNs. For 16,762 out of 23,721 AGNs, Ly $\alpha$  FWHM measurements are available from Rakshit et al. (2020). The other AGNs without FWHM measurement are removed owing to the poor quality of the Ly $\alpha$  line. We thus use these 16,762 AGNs with good quality of the Ly $\alpha$  line to compose our AGN sample, referred to as the All-AGN sample.

To investigate the type dependence, we classify these 16,762 AGNs into type 1 and type 2 AGNs. In the same manner as the T1-AGN(H) sample construction, we use Ly $\alpha$  line width measurements of Rakshit et al. (2020) for the type 1 and type 2 AGN classification. For the 16,762 AGNs, we apply the criterion of Ly $\alpha$  FWHM > 1000 km s<sup>-1</sup> (Panessa & Bassani 2002; Villarroel & Korn 2014) to select type 1 AGNs and obtain 14,693 type 1 AGNs. Following Panessa & Bassani (2002) and Villarroel & Korn (2014), we classify type 2 AGNs by the criterion of Ly $\alpha$  FWHM < 1000 km s<sup>-1</sup> and obtain 2069 type 2 AGNs (see Zakamska et al. 2003; Alexandroff et al. 2013). These type 1 and type 2 AGNs are referred to as T1-AGN and T2-AGN, respectively.

Table 1 presents the summary of foreground samples. We obtain 14,693 and 1829 type 1 AGNs, referred to as T1-AGN and T1-AGN(H), from SDSS and HETDEX, respectively. We select 2069 type 2 AGNs that are referred to as T2-AGN from SDSS.

# 3.3. Background Source Sample

In this subsection, we describe how the background sources are selected. We select the background sources with the SDSS DR16Q catalog, following the three steps below.

**Table 2** Sample Size of Background Sample at z = 2.08-3.67

Name of Sample	ExFall	ExSpring	Total	Survey	Criteria
Background AGNs	2181	12,555	14,736	SDSS	$\langle S/N \rangle_{Ly\alpha forest} > 1.4$

In the first step, we extract QSOs in our study field from the SDSS DR16Q catalog. We then select QSOs falling in the range of redshifts from 2.08 to 3.67. The lower and upper limits of the redshift range are determined by the Ly $\alpha$  forest. Our goal is to probe HI absorbers at z=2.0–3.0 with the Ly $\alpha$  forest. Because the Ly $\alpha$  forest is observed in the rest-frame 1040-1185 Å of the background sources, we obtain the lower and upper limits of the redshifts, 2.08 and 3.67, by  $1216 \times (1+2.0)/1185-1=2.08$  and  $1216 \times (1+3.0)/1040-1=3.67$ , respectively. By this step, we have selected 26,899 background source candidates.

In the second step, we choose background source candidates with good quality. We calculate the average signal-to-noise ratio,  $\langle S/N \rangle$ , in the wavelength range of the Ly $\alpha$  forest for the 26,899 background source candidates, and we select 15,573 candidates with  $\langle S/N \rangle$  greater than 1.4. To maximize the special resolution of the tomography map, we set the threshold,  $\langle S/N \rangle > 1.4$ , smaller than the value used by Mukae et al. (2020). This threshold is more conservative than the value of 1.2 used in Lee et al. (2018). In the third step, we remove damped Ly $\alpha$  absorbers (DLAs) and broad absorption lines (BALs) from the Ly $\alpha$  forest of the 15,573 candidates, because the DLAs and BALs cause an overestimation of the absorption of the Ly $\alpha$  forest. We identify and remove DLAs using the catalog of Chabanier et al. (2022), which is based on the SDSS DR16Q (Lyke et al. 2020). We mask out the wavelength ranges contaminated by the DLAs of the Chabanier et al. (2022) catalog (see Section 4.1 for the procedures). We conduct visual inspection for the 15,573 candidates to remove 115 BALs. In this way, we obtain 15,458 (=15,573-115) sources whose spectra are free from DLAs and BALs, which we refer to as the background source sample. Table 2 lists the number of background sources in each field.

#### 4. H I Tomography and Mapping

In this section we describe the process to construct HI tomography maps with the spectra of the background sources. For HI tomography, we need to obtain intrinsic continua of the background sources. Section 4.2 explains masking the biasing absorption features in the background sources, while Section 4.3 determines the intrinsic continua of the background source spectra. In Section 4.3, we construct HI tomography maps with the intrinsic continuum spectra.

#### 4.1. DLA and Intrinsic Absorption Masking

Because a DLA is an absorption system with a high neutral hydrogen column density  $N_{\rm HI} > 2 \times 10^{20}~{\rm cm}^{-2}$ , the intervening DLA completely absorbs a large portion of the Ly $\alpha$  forest over  $\Delta v \sim 10^3~{\rm km~s}^{-1}$ , which gives bias in the estimates of the intrinsic continua of the background sources. For the spectra of the background sources, we mask out the DLAs identified in Section 3.3. We determine the range of wavelengths for masking with the IDL code of Lee et al. (2012). The wavelength range corresponds to the EW of each DLA

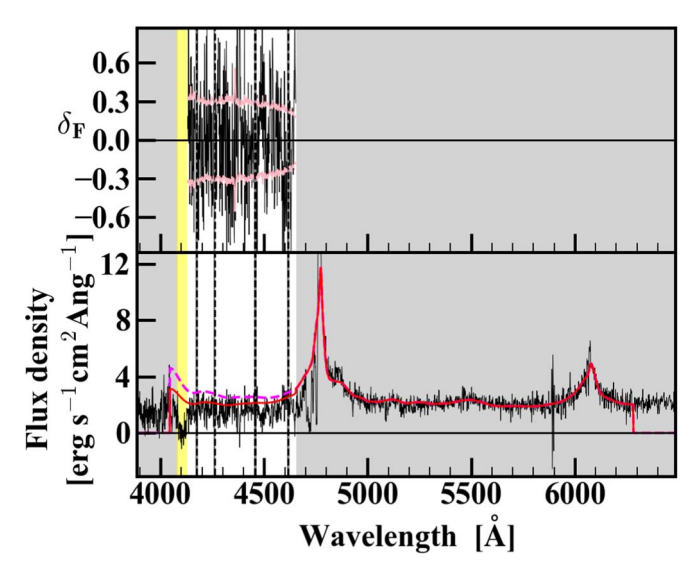


Figure 3. Example of a background source spectrum that was used for the reconstruction of the H I tomography map. Bottom panel: estimation of intrinsic continuum. The thin black line is the spectrum of a background source taken from SDSS. The red and magenta lines are the results of MF-PCA and PCA fitting, respectively. The vertical dashed lines present the central wavelengths of the metal absorptions. The gray hatches represent the wavelength ranges that are not used for the H I tomography map reconstructions. The yellow hatch indicates the wavelength ranges of DLA. Top panel: spectrum of  $\delta_F$  extracted from the bottom panel in the Ly $\alpha$  forest wavelength range. The vertical yellow and gray hatches are the same as those in the bottom panel. The black and pink lines show the spectrum of  $\delta_F$  and the error of  $\delta_F$  at the corresponding wavelength extracted from the bottom panel. The horizontal line indicates the cosmic average of Ly $\alpha$  forest transmission.

(Draine 2011):

$$W \sim \lambda_{\alpha} \left[ \frac{e^2}{m_{\rm e} c^2} N_{\rm HI} f_{\alpha} \lambda_{\alpha} \left( \frac{\gamma_{\alpha} \lambda_{\alpha}}{c} \right) \right]^{1/2}$$
. (2)

In the formula,  $\lambda_{\alpha}$  is the rest-frame wavelength of the hydrogen Ly $\alpha$  line (i.e., 1216 Å), while c, e,  $m_e$ ,  $f_{\alpha}$ ,  $N_{\rm HI}$ , and  $\gamma_{\alpha}$  are the speed of light, the electron charge, the electron mass, the Ly $\alpha$  oscillator strength, the H I column density of the DLA, and the sum of the Einstein A-coefficients. We mask out these wavelength ranges of the background source spectra. In Figure 3, the masked DLA is indicated by yellow hatches.

We also mask out the intrinsic absorption lines of the metal absorption lines, which are the other sources of bias. We mask SIV  $\lambda 1062$ , N II  $\lambda 1084$ , N I  $\lambda 1134$ , and C III  $\lambda 1176$  (Lee et al. 2012), which are shown by the dashed lines in Figure 3. Because the spectral resolutions of SDSS DR14Q are  $\Delta\lambda = 1.8-5.2$  Å, we adopt the masking size of 10 Å in the observed frame.

## 4.2. Intrinsic Continuum Determination

In order to obtain the intrinsic continuum of the background source (Section 3.3) in the Ly $\alpha$  forest wavelength range (rest-frame 1040–1185 Å), we conduct mean-flux regulated PCA

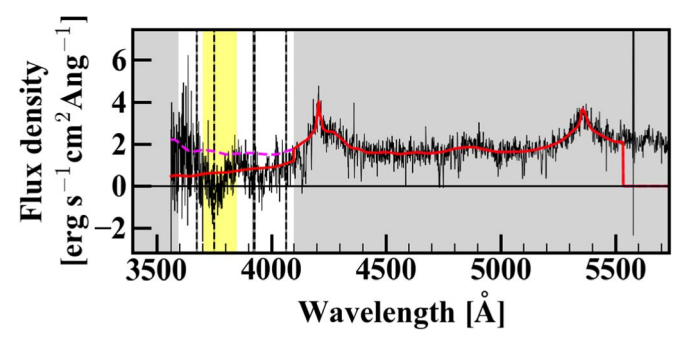


**Figure 4.** Same as the bottom panel of Figure 3, but for the background spectrum with a poor fitting result. The red and magenta lines are the results of MF-PCA and PCA continuum fitting, respectively. The yellow hatch indicates the wavelength range of unknown absorption.

(MF-PCA) fitting with the IDL code (Lee et al. 2012) for the background sources after the masking (Section 4.1).

There are two steps in the MF-PCA fitting process. The first step is to predict the shape of the intrinsic continuum of the background sources in the Ly $\alpha$  forest wavelength range. We conduct least-squares PCA fitting (Suzuki et al. 2005; Lee et al. 2012) to the background source spectrum in the rest-frame 1216–1600 Å,

$$f_{\text{PCA}}(\lambda) = \mu(\lambda) + \sum_{i=1}^{8} c_i \xi_j(\lambda), \tag{3}$$

where  $\lambda$  is the rest-frame wavelength. The values of  $c_j$  are the free parameters for the weights. The function of  $\mu(\lambda)$  is the average spectrum calculated from the 50 local QSO spectra in Suzuki et al. (2005). The function of  $\xi_j(\lambda)$  represents the *j*th principle component (or "eigenspectrum") out of the eight principle components taken from the PCA template derived by Suzuki et al. (2005).

In the second step, we predict the intrinsic continuum of the background source in the Ly $\alpha$  forest wavelength range. Because the PCA template is obtained with the local QSO spectra, the best-fit  $f_{\rm PCA}$  in the Ly $\alpha$  forest does not include cosmic evolution on the average transmission rate. On average, the best-fit  $f_{\rm PCA}$  in the Ly $\alpha$  forest should agree with the cosmic mean-flux evolution (Faucher-Giguère et al. 2008c)

$$\langle F(z) \rangle = \exp[-0.001845(1+z)^{3.924}],$$
 (4)

where z is the redshift of the absorber. We use  $f_{PCA}$  and a correction function of  $a+b\lambda$  to estimate the intrinsic continuum  $f_{\text{intrinsic}}(\lambda)$  for large-scale power along the LOS with the equation

$$f_{\text{intrinsic}}(\lambda) = f_{\text{PCA}}(\lambda) \times (a + b\lambda),$$
 (5)

where a and b are the free parameters. Because the ratio of  $f_{\rm obs}(\lambda)/f_{\rm intrinsic}(\lambda)$  should agree with the cosmic average  $\langle F(z) \rangle$  for  $z=(\lambda/1216)-1$  in the wavelength range of the Ly $\alpha$  forest, we conduct least-squares fitting to find the values of a and b providing the best fit between the mean ratio and the cosmic average. The red line shown by the bottom panel of Figure 3 presents an MF-PCA fitted continuum derived from the spectrum of one of our background sources.

By the MF-PCA fitting, we have obtained the estimates of  $f_{\rm intrinsic}(\lambda)$  for 14,736 out of 15,458 background sources. We find that the other background sources show poor fitting results

found by visual inspection. We do not use these background sources in the following analyses. Figure 4 shows an example of a poor fitting result due to the unknown absorption. We adopt continuum fitting errors of  $\sim$ 7%,  $\sim$ 6%, and  $\sim$ 4% for Ly $\alpha$  forests with mean S/N values of <4, 4–10, and >10, respectively (Lee et al. 2012).

#### 4.3. HI Tomography Map Reconstruction

We reconstruct our H I tomography maps by a procedure similar to Lee et al. (2018). We define Ly $\alpha$  forest fluctuations  $\delta_F$  at each pixel on the spectrum by

$$\delta_F = \frac{f_{\text{obs}}/f_{\text{intrinsic}}}{\langle F(z) \rangle} - 1, \tag{6}$$

where  $f_{\rm obs}$  and  $f_{\rm intrinsic}$  are the observed spectrum and estimated intrinsic continuum, respectively.  $\langle F(z) \rangle$  is the cosmic average transmission. We calculate  $\delta_F$  with our background source spectra. The top panel of Figure 3 shows the "spectrum" of  $\delta_F$  derived from the  $f_{\rm obs}$  and  $f_{\rm intrinsic}$  in the bottom panel. For the pixels in the wavelength ranges of masking (Section 4.1), we do not use  $\delta_F$  in our further analyses. We thus obtain  $\delta_F$  in 876,560 pixels.

For the the H I tomography map of the Extended Fall field, we define the cells of the H I tomography map in the 3D comoving space. We choose a volume of  $30^{\circ} \times 3^{\circ}.3$  in the longitudinal and latitudinal dimensions, respectively, in the redshift range of 2.0 < z < 3.0. The comoving size of our H I tomography map is  $2257\ h^{-1}\ \text{cMpc} \times 233\ h^{-1}\ \text{cMpc} \times 811\ h^{-1}\ \text{cMpc}$  in the R.A., decl., and z directions, respectively, in the same manner as Mukae et al. (2020). Our H I tomography map has  $451 \times 46 \times 162\ \text{cells}$ , and one cell is a cube with a size of  $5.0\ h^{-1}\ \text{cMpc}$  on a side, where the LOS distance is estimated under the assumption of the Hubble flow.

We conduct a Wiener filtering scheme for reconstructing the sight lines that do not have background sources. We use the calculation code developed by Stark et al. (2015). The solution for each cell of the reconstructed sight line is obtained by

$$\delta_F^{\text{rec}} = C_{\text{MD}} \cdot (C_{\text{DD}} + N)^{-1} \cdot \delta_F, \tag{7}$$

where  $C_{\rm MD}$ ,  $C_{\rm DD}$ , and N are the map—data, data—data, and noise covariances, respectively. We assume Gaussian covariances between two points  $r_1$  and  $r_2$ :

$$C_{\text{MD}} = C_{\text{DD}} = C(r_1, r_2),$$
 (8)

$$C(r_1, r_2) = \sigma_F^2 \exp \left[ -\frac{(\Delta r_{\parallel})^2}{2L_{\parallel}^2} \right] \exp \left[ -\frac{(\Delta r_{\perp})^2}{2L_{\perp}^2} \right],$$
 (9)

where  $\Delta r_{\parallel}$  and  $\Delta r_{\perp}$  are the distances between  $r_1$  and  $r_2$  in the directions of parallel and transverse to the LOS, respectively. The values of  $L_{\perp}$  and  $L_{\parallel}$  are the correlation lengths for vertical and parallel to the LOS direction, respectively, and defined with  $L_{\perp} = L_{\parallel} = 15~h^{-1}~\text{cMpc}$ . The value of  $\sigma_F^2$  is the normalization factor that is  $\sigma_F^2 = 0.05$ . Stark et al. (2015) develop this Gaussian form to obtain a reasonable estimate of the true correlation function of the Ly $\alpha$  forest. We perform the Wiener filtering reconstruction with the values of  $\delta_F$  at the 898,390 pixels, using the aforementioned parameters of the Stark et al. (2015) algorithm with a stopping tolerance of  $10^{-3}$  for the preconditioned conjugation gradient solver. As noted by

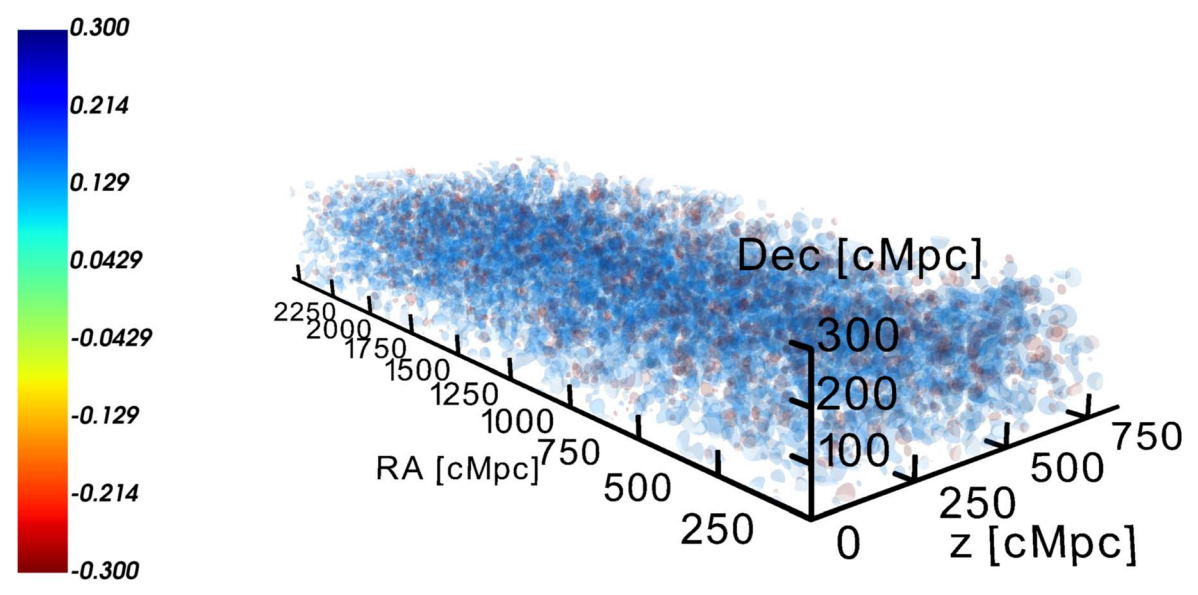


Figure 5. 3D H I tomography map of the ExFall field. The color contours represent the values of  $\delta_F$  from negative (red) to positive (blue). The spatial volume of the H I tomography map is  $2257 \times 233 \times 811 \ h^{-3} \ \text{cMpc}^3$ . The redshift range is z = 2.0 - 3.0.

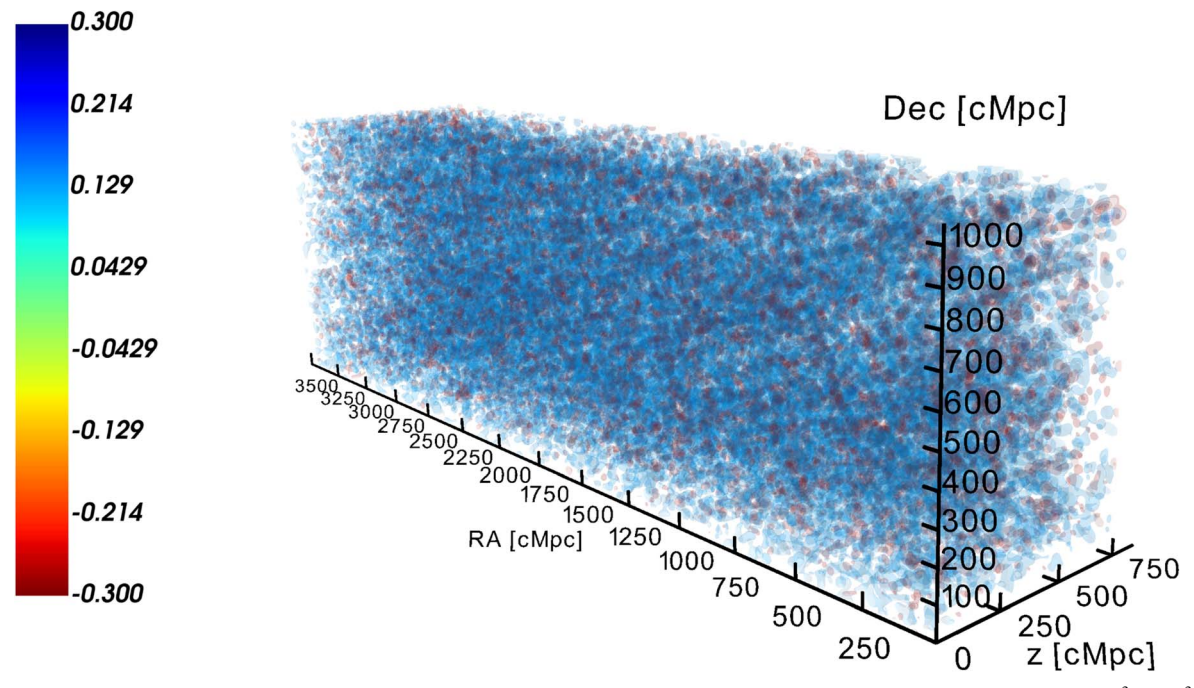


Figure 6. Same as Figure 5, but for the ExSpring field. The spatial volume of the H I tomography map is  $3475 \times 1058 \times 811 \ h^{-3}$  cMpc<sup>3</sup>.

Lee et al. (2016), the boundary effect that leads to an additional error on  $\delta_F$  occurs at the positions that are near the boundaries of an H I tomography map. The boundary effect is caused by the background sight lines not covering the region that contributes to the calculation of the  $\delta_F$  values for cells near the H I tomography map boundaries. To avoid the boundary effect, we extend a distance of  $40~h^{-1}$  cMpc for each side of the H I tomography map of the ExFall field. The resulting map is shown in Figure 5.

For the H I tomography map reconstruction of the Extended Spring field (hereafter ExSpring field), we perform almost the same procedure as the one of the ExFall field. The area of the ExSpring field is more than 6 times larger than that of the ExFall field. We separate the ExSpring field into  $8 \times 3 = 24$ 

footprints to save calculation time. Each footprint covers an area of  $10^{\circ} \times 5^{\circ}$  in the R.A. and decl. directions, respectively. We reconstruct the H I tomography map one by one for the footprints of the ExSpring field.

To weaken the boundary effect, we extend a distance of  $40\ h^{-1}$  cMpc for each side of the footprints. The extensions mean that every two adjacent footprints have an overlapping region of  $80\ h^{-1}$  cMpc width. The width of the overlapping regions is a conservative value to weaken the boundary effect since it is much larger than the resolution,  $15\ h^{-1}$  cMpc, of our H I tomography maps. By the  $40\ h^{-1}$  cMpc extension, we reduce the uncertainty in the  $\delta_F$  value for the edge of each footprint caused by the boundary effect to  $\pm 0.01$ . This value corresponds to 1/10 of the typical error for each cell of the H I tomography map (Mukae et al. 2020). The remaining

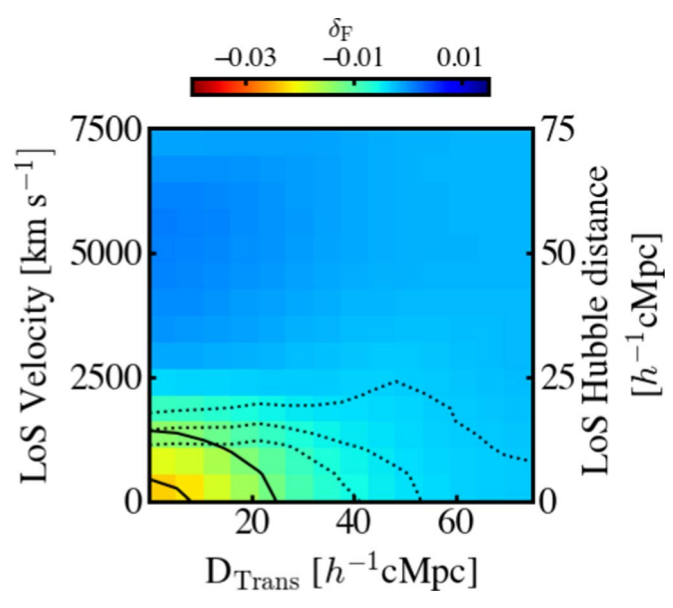


**Figure 7.** 2D H I profile of the All-AGN sample sources. The color map indicates the  $\delta_F$  values of each cell of the 2D H I profile. The solid lines denote constant  $\delta_F$  values in steps of -0.01 starting at -0.01. The dotted lines correspond to multiples of  $3\sigma$  starting at  $6\sigma$ .

additional error caused by the boundary effect is negligible compared to the statistical uncertainties in the H I distributions obtained in Section 5. Then, we follow the reconstruction procedure for the ExFall field to reconstruct H I tomography maps of the footprints and cut off all the cells within  $40\ h^{-1}$  cMpc to the borders that are affected by the boundary effect. Finally, we obtain the H I tomography map of the ExSpring field with a special volume of  $3475\ h^{-1}$  cMpc  $\times$   $1058\ h^{-1}$  cMp

#### 5. Results and Discussions

# 5.1. Average H I Profiles around AGNs: Validations of our AGN Samples

In this section we present the H I profile,  $\delta_F$ , as a function of distance, with the All-AGN sample sources, using the reconstructed H I tomography maps. We compare the H I profile of the All-AGN sample to the one of the previous study (Font-Ribera et al. 2013). We also present the comparison of the H I profiles between T1-AGN(H) and T1-AGN samples that are made with the HETDEX and SDSS data. In this study, we only discuss the structures having size  $\gtrsim 15~h^{-1}$  cMpc corresponding to the resolution of our 3D H I tomography maps.

For the H I profiles with the All-AGN sample, we extract  $\delta_F$  values around the 16,978 All-AGN sample sources in the H I tomography map. We cut the H I tomography map centered at the positions of the All-AGN sample sources and stack the  $\delta_F$  values to make a two-dimensional (2D) map of the average  $\delta_F$  distribution around the sources that is referred to as a 2D H I profile of the All-AGN sample sources. The two dimensions of the 2D H I profile correspond to the transverse distance  $D_{\text{Trans}}$  and the LOS Hubble distance. The velocity corresponding to the LOS Hubble distance is referred to as the LOS velocity.

Figure 7 shows the 2D H I profile with values of  $\delta_F$  for the All-AGN sample. The solid black lines denote the contours of  $\delta_F$ . In each cell of the 2D H I profile, we define the  $1\sigma$  error

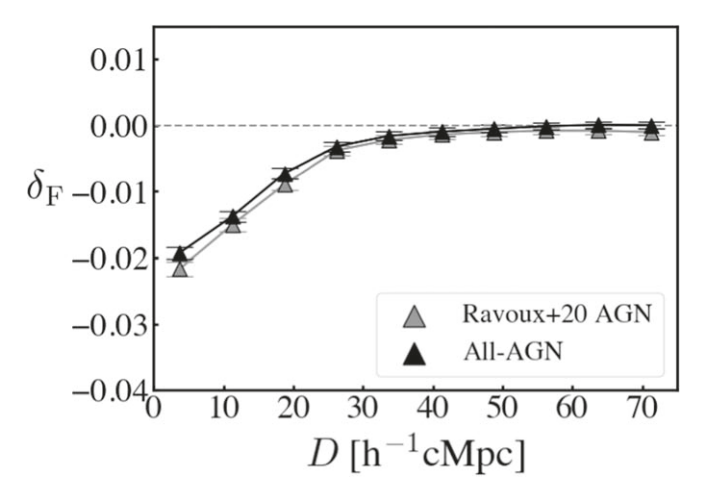


**Figure 8.** H I radial profile of the All-AGN and Ravoux et al. (2020) AGN samples. The black and gray data points and error bars show the H I radial profiles of our All-AGN sample sources and the AGNs of Ravoux et al. (2020), respectively. The horizontal dashed line shows the cosmic average Ly $\alpha$  transmission fluctuation,  $\delta_F = 0$ .

with the standard deviation of  $\delta_F$  values of the 100 mock 2D H I profiles. Each mock 2D H I profile is obtained in the same manner as the real 2D H I profile, but with random positions of sources whose number is the same as the one of All-AGN sample sources. In Figure 7, the dotted black lines indicate the contours of the  $6\sigma$ ,  $9\sigma$ , and  $12\sigma$  confidence levels, respectively. We find the  $19.5\sigma$  level detection of  $\delta_F$  at the source position (0,0). The  $\delta_F$  value at the source position indicates the averaging value over the ranges of  $(-7.5 \ h^{-1} \ \text{cMpc})$ ,  $+7.5 \ h^{-1} \ \text{cMpc})$  in both the LOS and transverse directions. The  $19.5\sigma$  level detection at the source position is suggestive that obvious  $\text{Ly}\alpha$  forest absorption exists near the All-AGN sources on average. The 2D H I profile is more extended in the transverse direction than along the LOS. We discuss this difference in Section 5.2.

We then define a 3D distance, D, under the assumption of the Hubble flow in the LOS direction. We derive  $\delta_F$  as a function of D that is referred to as "HI radial profile," averaging  $\delta_F$  values of the 2D HI profile over the 3D distance. Figure 8 shows the HI radial profile of the All-AGN sample. We find that the  $\delta_F$  values increase toward a large distance. This trend is consistent with the one found by Ravoux et al. (2020) with the SDSS quasars.

Ravoux et al. (2020) have obtained the average Ly $\alpha$ transmission fluctuation distribution around the AGNs taken from the SDSS data release 16 quasar (SDSS DR16Q) catalog in the field of Strip 82. The criteria of the target selection for the SDSS DR16Q and SDSS DR14Q sources are the same. The luminosity distribution of AGNs for Ravoux et al. (2020) is almost the same as that of our All-AGN sample sources that are taken from the SDSS DR14Q catalog. We derive the average radial H I profile of the Ravoux et al. (2020) AGN sources by the same method as for our All-AGN sample, using the 3D H I tomography map reconstructed by Ravoux et al. (2020). We compare the radial H I profile of the All-AGN sample with the one derived from the 3D H I tomography map of Ravoux et al. (2020). The comparison is shown in Figure 8. Our result agrees with that of Ravoux et al. (2020) within the error range at scale  $D > 10 h^{-1}$  cMpc. The peak values of  $\delta_F$  showing the strongest Ly $\alpha$  absorption are comparable,  $\delta_F \simeq -0.02$ . The slight difference between the peak values of our results and those of Ravoux et al. can be explained by the different approaches

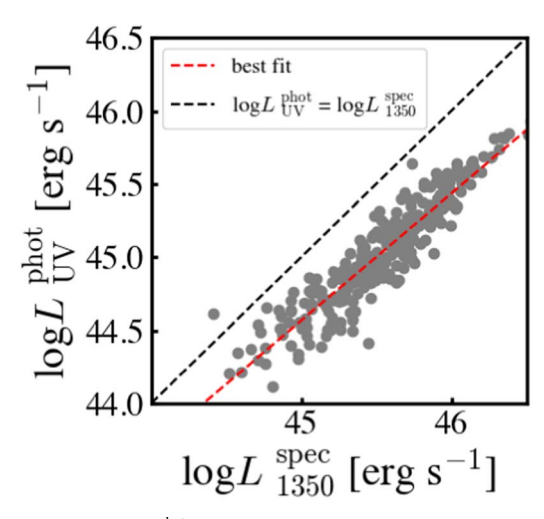


**Figure 9.** Relations of  $L_{\rm UV}^{\rm phot}$  against  $L_{\rm 1350}^{\rm spec}$  for the sources categorized in both the T1-AGN(H) and T1-AGN samples. The  $L_{\rm UV}^{\rm phot}$  and  $L_{\rm 1350}^{\rm spec}$  are measured from the HSC r-band imaging and SDSS spectra (Rakshit et al. 2020), respectively. The gray points show the distribution of  $L_{\rm 1350}^{\rm spec} - L_{\rm UV}^{\rm phot}$  relations for the sources categorized in both the T1-AGN(H) and T1-AGN samples. The black dashed line indicates the relation where  $L_{\rm 1350}^{\rm spec} = L_{\rm UV}^{\rm phot}$ . The red dashed line represents the linear best fit of the blue points.

of the estimation for the intrinsic continuum adopted by Ravoux et al. and us. Ravoux et al. conduct power-law fitting, which is different from the MF-PCA fitting that we used, for the intrinsic continuum in the wavelength range of the Ly $\alpha$  forest. Given the low ( $\sim$ 15  $h^{-1}$ ) spatial resolution of both our H I tomography map and that of Ravoux et al. (2020), neither study is able to search for the proximity effect making a photoionization region around AGNs (D'Odorico et al. 2008). From the comparison shown by Figure 8, we conclude that the Ly $\alpha$  forest absorption derived from our H I tomography map is reliable.

To check the reliability of the HETDEX survey results, we use the reliable result of the SDSS AGNs to compare with the result derived by the HETDEX AGNs.

We select type 1 AGNs from HETDEX's T1-AGN(H) and SDSS's T1-AGN samples to make subsamples of T1-AGN(H) and T1-AGN with matching rest-frame 1350 Å luminosity  $(L_{1350})$ . For T1-AGN, the measurements directly from the SDSS spectra ( $L_{1350}^{\text{spec}}$ ) are available (Rakshit et al. 2020). For T1-AGN(H), we do not have  $L_{1350}^{\text{spec}}$  measurements from the HETDEX spectra, so we estimate it using HSC r-band imaging. Since the central wavelength of the r-band imaging is rest-frame  $\sim 1700$  Å, we calibrate the conversion between r-band luminosity,  $L_{\rm UV}^{\rm phot}$ , and  $L_{1350}^{\rm spec}$ . We examine the 283 type 1 AGN sources that appear in both SDSS and HETDEX (and, thus, have both  $L_{1350}^{\text{spec}}$  measurements from SDSS and r-band luminosities from HSC) to calibrate the relationship. The results are displayed in Figure 9. The  $L_{\rm UV}^{\rm phot}$  are always smaller than those of  $L_{1350}^{\rm spec}$  (Rakshit et al. 2020). Due to the blue UV slope of the spectra for the AGNs categorized in both the T1-AGN(H) and T1-AGN samples, the luminosity of the restframe 1350 Å always shows a larger value than the one of restframe 1700 Å. We conduct linear fitting to the data points of Figure 9 and obtain the best-fit linear function. With the best-fit linear function, we estimate  $L_{1350}^{\text{spec}}$  values for HETDEX's T1-AGN(H) sample sources.

We show the  $L_{1350}^{\text{spec}}$  distributions of all the T1-AGN(H) and T1-AGN sample sources in the top panel of Figure 10. The

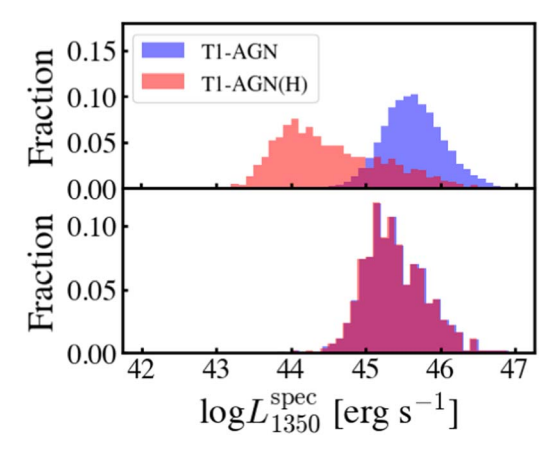


**Figure 10.** Top panel: L<sub>1350</sub> distributions of the T1-AGN and T1-AGN(H) samples with blue and red histograms, respectively. Bottom panel: same as the top panel, but for the T1-AGN and T1-AGN(H) subsample sources.

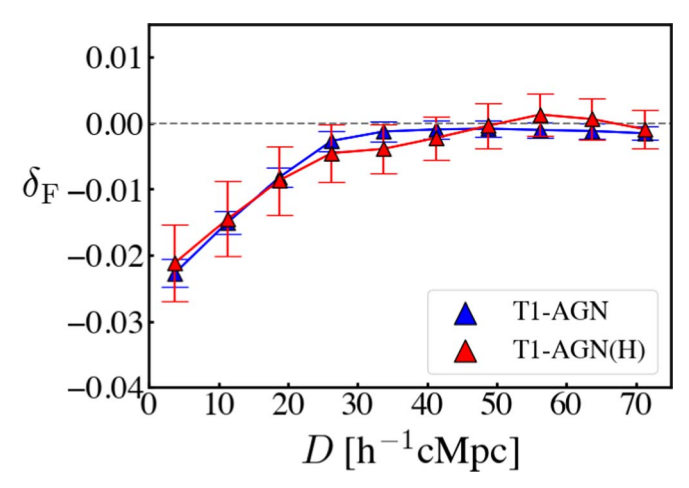


**Figure 11.** H I radial profiles of the T1-AGN and T1-AGN(H) subsamples. The blue and red triangles show the values of  $\delta_F$  as a function of distance, D, for the T1-AGN and T1-AGN(H) sample sources, respectively. The horizontal dashed line shows the cosmic average Ly $\alpha$  transmission fluctuation,  $\delta_F = 0$ .

 $L_{1350}^{\rm spec}$  distribution of T1-AGN(H) covers a wider luminosity range than the one of T1-AGN. To make sure the comparison between the SDSS and HETDEX AGNs is fair, we make the subsamples of T1-AGN and T1-AGN(H) that consist of the sources with matching  $L_{1350}^{\rm spec}$  distributions. We present the  $L_{1350}^{\rm spec}$  distributions of the T1-AGN and T1-AGN(H) subsamples in the bottom panel of Figure 10. We obtain 540 and 4338 type 1 AGNs for the subsamples of T1-AGN(H) and T1-AGN, respectively, whose  $L_{1350}^{\rm spec}$  distributions are shown in the bottom panel of Figure 9.

We derive the H I radial profiles for the subsamples of T1-AGN(H) and T1-AGN sample sources, as shown in Figure 11. The H I radial profiles of T1-AGN(H) and T1-AGN subsample sources are in good agreement.

# 5.2. AGN Average Line-of-sight and Transverse H I Profiles

Based on the 2D H I profile of the All-AGN sample (Figure 7), we find that the Ly $\alpha$  forest absorptions of the All-AGN sample sources are more extended in the transverse direction. In this section, we present the H I radial profiles of

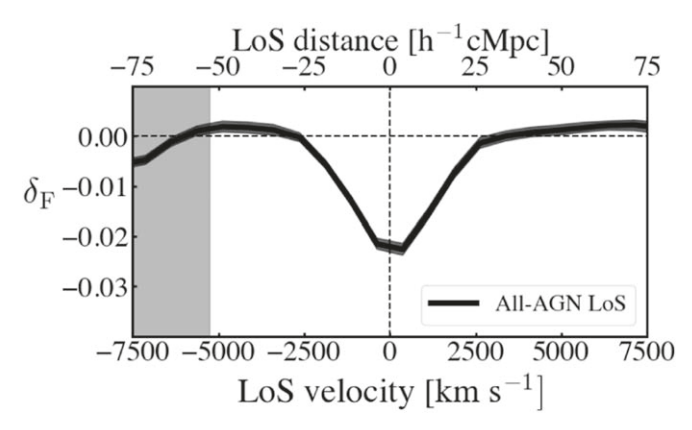


**Figure 12.** H I radial profiles of LOS velocity (LOS distance) for the All-AGN sample. The black solid line shows the  $\delta_F$  values as a function of LOS velocity (LOS distance) for the All-AGN sample. The vertical dashed line presents the position of LOS velocity  $= 0 \text{ km s}^{-1}$  (LOS distance  $= 0 \text{ } h^{-1} \text{ cMpc}$ ). The horizontal dashed line indicates the cosmic average Ly $\alpha$  transmission fluctuation,  $\delta_F = 0$ . The gray shaded area shows the range of the  $\delta_F$  not used to derive the LOS H I radial profile.

the All-AGN sample in the LOS and transverse directions and compare these two H I radial profiles.

To derive the H I radial profile of the All-AGN sample with the absolute LOS distance, which is referred to as the LOS HI radial profile (Figure 13), we average  $\delta_F$  values of the 2D H I profiles of All-AGN over  $D_{\text{Trans}} < 7.5 \ h^{-1}$  cMpc (from  $-7.5 \ h^{-1}$  cMpc to  $+7.5 \ h^{-1}$  cMpc in the transverse direction), which corresponds to the spatial resolution of the 2D H I profile map,  $15 h^{-1}$  cMpc. Among the 16,978 All-AGN sample sources, 10,884 are used as both background and foreground sources. In this case, the Ly $\alpha$  transmission fluctuation ( $\delta_F$ ) of these 10,884 sources at the LOS velocity  $\lesssim -5250 \text{ km s}^{-1}$  is estimated mainly from their own spectrum. As discussed in Youles et al. (2022), the redshift uncertainty of the SDSS AGNs causes the overestimation of intrinsic continuum and the underestimation of  $\delta_F$  around metal emission lines such as C III  $\lambda 1176$ . This leads to a systemic error toward negative  $\delta_F$  in the HI radial profile of LOS velocity (LOS distance) at LOS velocities  $\lesssim 5250 \text{ km s}^{-1}$  (Figure 12). The H I radial profile of LOS velocity (LOS distance) is derived by averaging  $\delta_F$  values over  $D_{\text{Trans}} < 7.5 \ h^{-1}$  cMpc as a function of the negative and positive LOS velocity (LOS distance). In this study, we only use the values of  $\delta_F$  at LOS distances  $> -52.5 \ h^{-1}$  cMpc (LOS velocities  $> -5250 \text{ km s}^{-1}$ ) to derive the LOS H I radial profile of the All-AGN sample (Figure 13). The scale, LOS distances  $> -52.5 \ h^{-1} \ \text{cMpc} \ (\text{LOS} \ \text{velocities} \ > -5250 \ \text{km s}^{-1}), \text{ is}$ determined by the maximum wavelength of the Ly $\alpha$  forest we used, the smoothing scale of the Wiener filtering scheme, and the AGN redshift uncertainty, assumed by Youles et al. (2022). After removing the  $\delta_F$  values affected by the systemics in the 2D H I profile, we present the LOS H I radial profile of the All-AGN sample in Figure 13.

We estimate the H I radial profiles of  $D_{\rm Trans}$ , which is referred to as the transverse H I radial profile, by averaging the  $\delta_F$  values over the LOS velocity of (-750, +750) km s<sup>-1</sup>, whose velocity width corresponds to 15  $h^{-1}$  cMpc in the Hubble flow distance. The H I radial profile of  $D_{\rm Trans}$  is also shown in Figure 13.

We compare the LOS and transverse H I radial profiles. The  $\delta_F$  values increase toward large scale more rapidly in the LOS direction than those in the transverse direction (Figure 13). This

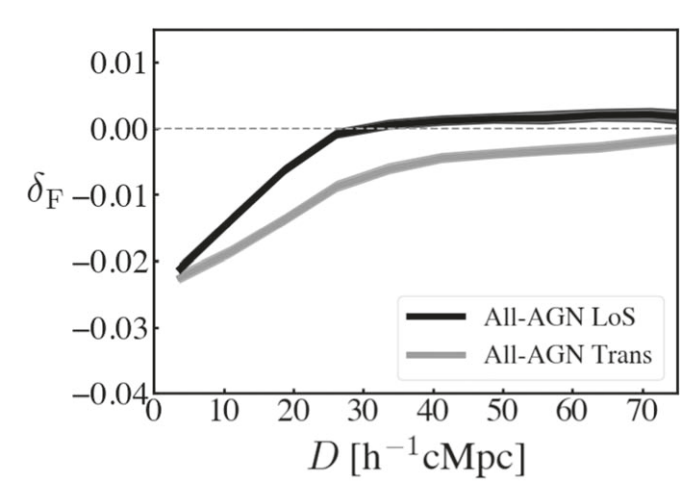


**Figure 13.** LOS and transverse H I radial profiles of the All-AGN sample. The black and gray lines show the  $\delta_F$  values as a function of LOS distance and  $D_{\rm Trans}$ , respectively. The horizontal dashed line indicates  $\delta_F=0$ .

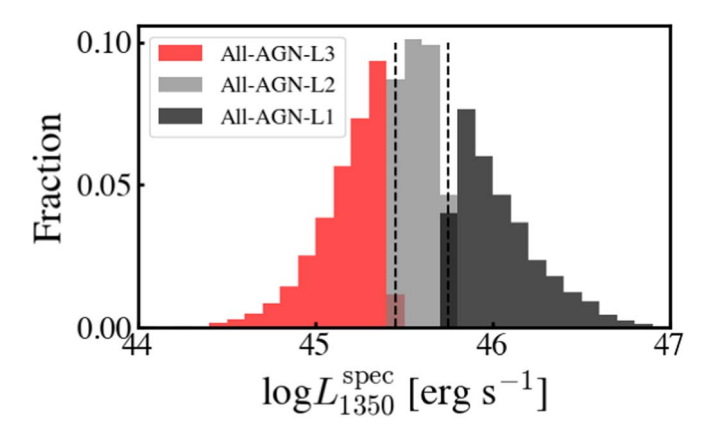


**Figure 14.**  $\log L_{1350}^{\rm spec}$  distribution of the bright and All-AGN sample sources. The vertical dashed lines indicate the borders of  $L_{1350}^{\rm spec}$  where  $\log (L_{1350}^{\rm spec}/[{\rm erg~s^{-1}}]) = 45.41$  and 45.75, respectively. These three borders separate the All-AGN sample into three subsamples of All-AGN-L3, All-AGN-L2, and All-AGN-L1, respectively.

difference may be explained by an effect similar to the Kaiser effect (Kaiser 1987), Doppler shifts in AGN redshifts are caused by the large-scale coherent motions of the gas toward the AGN. The LOS HI radial profile is positive,  $\delta_F \sim 0.002 \pm 0.0008$ , at large scales,  $\gtrsim 30~h^{-1}$  cMpc. In Section 5.5, we discuss the positive  $\delta_F$  values of LOS HI radial profiles at large scales and compare our observational result to the models of a previous study, Font-Ribera et al. (2013).

# 5.3. Source Dependences of the AGN Average HI Profiles

In this section, we present 2D and H I radial profiles of the AGN subsamples to investigate how the average H I density depends on luminosity and AGN type.

#### 5.3.1. AGN Luminosity Dependence

We study the AGN luminosity dependence of the average H I profiles. Figure 14 presents the  $L_{1350}^{\rm spec}$  distribution of All-AGN. We make three subsamples of All-AGN: All-AGN-L3, All-AGN-L2, and All-AGN-L1. The luminosity ranges of the subsamples are  $43.70 < \log(L_{1350}^{\rm spec}/[{\rm erg~s^{-1}}]) < 45.41$ ,  $45.41 < \log(L_{1350}^{\rm spec}/[{\rm erg~s^{-1}}]) < 45.75$ , and  $45.75 < \log(L_{1350}^{\rm spec}/[{\rm erg~s^{-1}}]) < 47.35$ ,

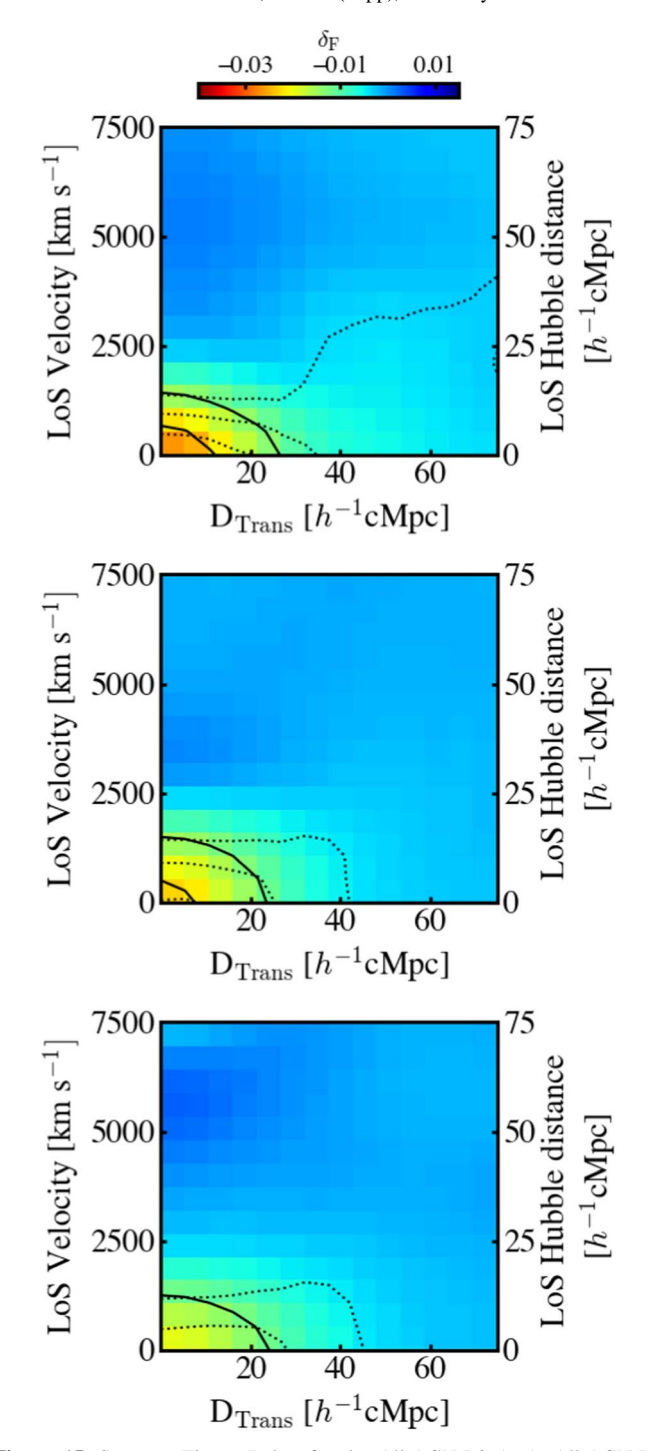


**Figure 15.** Same as Figure 7, but for the All-AGN-L3 (top), All-AGN-L2 (middle), and All-AGN-L1 (bottom) samples.

respectively. The luminosity ranges of the three subsamples are defined in a way that the number of AGNs is the same (5695) in each subsample. We derive the 2D H I profiles of the subsamples in the same manner as in Section 5.1, and we present the profiles in Figure 15. In these 2D H I profiles, the brightest subsample of All-AGN-L1 (the faintest subsample of All-AGN-L3) shows the weakest (the strongest) Ly $\alpha$  transmission fluctuations around the source position, D=0.

We then extract the HI radial profiles from the 2D HI profiles of the All-AGN subsamples, and we present the HI radial profiles in Figure 16. In this figure, we find that the peak

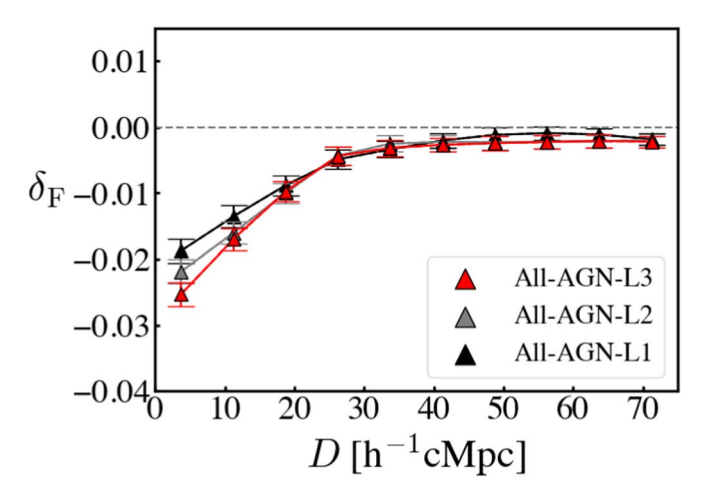


**Figure 16.** Same as Figure 11, but for the All-AGN-L3 (red), All-AGN-L2 (gray), and All-AGN-L1 (black) samples.

values of  $\delta_F$  for the All-AGN subsamples are anticorrelated with AGN luminosities. The peak  $\delta_F$  values near the source position drop from the faintest All-AGN-L3 subsample to the brightest All-AGN-L1 subsample. The gas densities around bright AGNs are higher than (or comparable to) those around faint AGNs; this result would suggest that the ionization fraction of the hydrogen gas around bright AGNs is higher than the one around faint AGNs on average.

We also present the LOS and transverse H I radial profiles of the All-AGN subsamples derived by the same method as that for the All-AGN sample in Figure 17. Similar to what we found in the comparison of the H I radial profiles for the All-AGN subsamples, the peak values of the LOS and transverse H I profiles also decrease from the faintest subsample, All-AGN L3, to the brightest subsample, All-AGN L1. For the LOS (transverse) H I radial profiles at the scales beyond 25  $h^{-1}$  cMpc, we do not find any significant differences in the comparison of the LOS (transverse) H I radial profiles for the All-AGN subsamples.

#### 5.3.2. AGN Type Dependence

We investigate the dependence of H I profiles on type 1 and type 2 AGNs. To remove the effects of the AGN luminosity dependence (Section 5.3.1), we make subsamples of T1-AGN and T2-AGN with the same  $L_{1350}^{\rm spec}$  distribution by the same manner as the one we conduct for the selection of T1-AGN and T1-AGN(H) subsamples in Section 5.1. The top panel of Figure 18 presents the  $L_{1350}^{\rm spec}$  distributions of T1-AGN and T2-AGN samples, while the bottom panel of Figure 18 shows those of the T1-AGN and T2-AGN subsamples. The subsamples of T1-AGN and T2-AGN are composed of 10,329 type 1 AGNs and 1462 type 2 AGNs, respectively. We derive the 2D H I profiles from the T1-AGN and T2-AGN subsamples. The profiles are presented in Figure 19. We find  $17.7\sigma$  and  $7.9\sigma$  detections at the source center position (0,0) of the T1-AGN and T2-AGN subsamples, respectively. We calculate the HI radial profiles from the 2D HI profiles of the T1-AGN and T2-AGN subsamples. In Figure 20, we compare the HI radial profiles of the T1-AGN and T2-AGN subsamples. No notable difference is found within  $1\sigma$  error. The peak value of  $\delta_F = 0$  of the T2-AGN subsample is within  $1\sigma$  error of the peak value of the T1-AGN subsample near the source position.

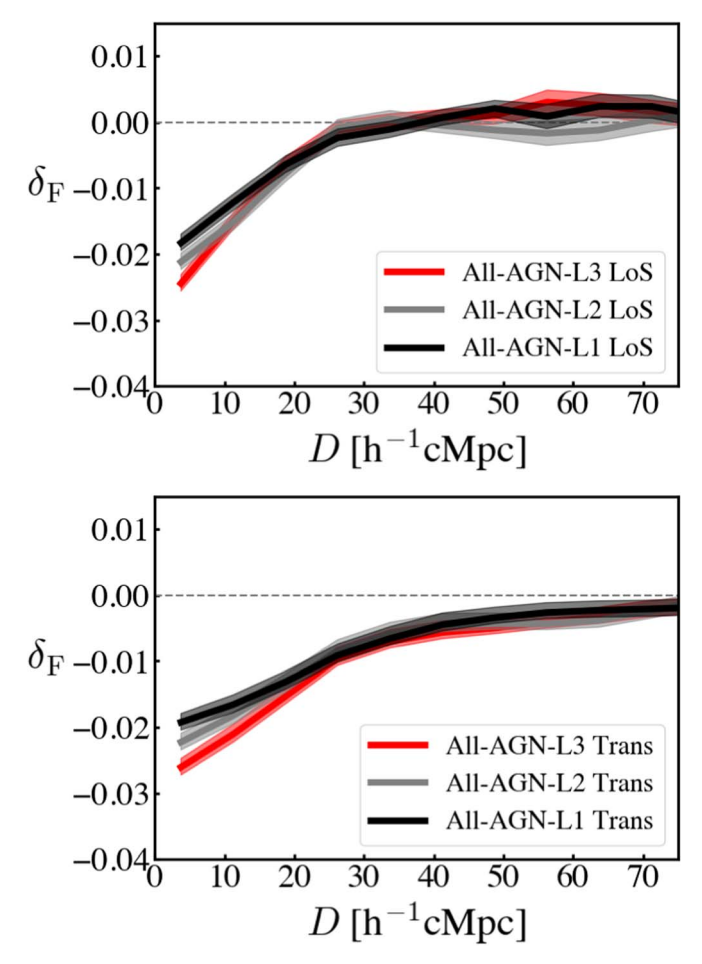


**Figure 17.** LOS and transverse H I radial profiles of the All-AGN-L3, All-AGN-L2, and All-AGN-L1 subsamples. The top panel (bottom panel) presents the LOS (transverse) H I radial profiles of the All-AGN-L3, All-AGN-L2, and All-AGN-L1 subsamples, shown by the red, gray, and black lines, respectively. The meaning of the horizontal dashed lines in both the top and bottom panels is the same as that in Figure 8.

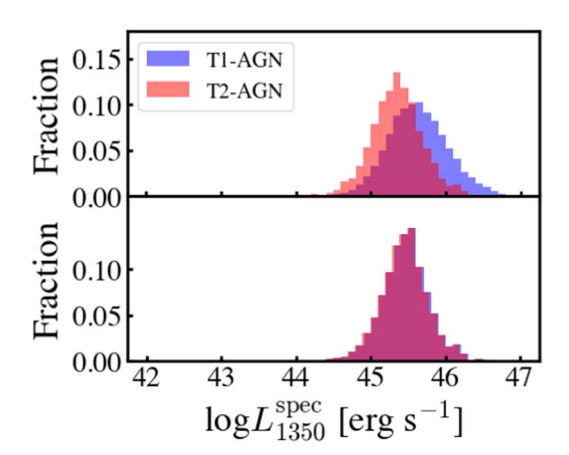


Figure 18. Same as Figure 10, but for the T1-AGN (blue) and T2-AGN (red) samples.

To compare the Ly $\alpha$  forest absorptions of type 1 and type 2 AGNs in the LOS and transverse directions, we derive the LOS and transverse H I radial profiles of the T1-AGN and T2-AGN subsamples, and we present the profiles in Figure 21. Similar to the trend of the H I radial profiles, the peak values of the LOS and transverse H I radial profiles for T1-AGN and T2-AGN subsamples are not significantly different. The comparable

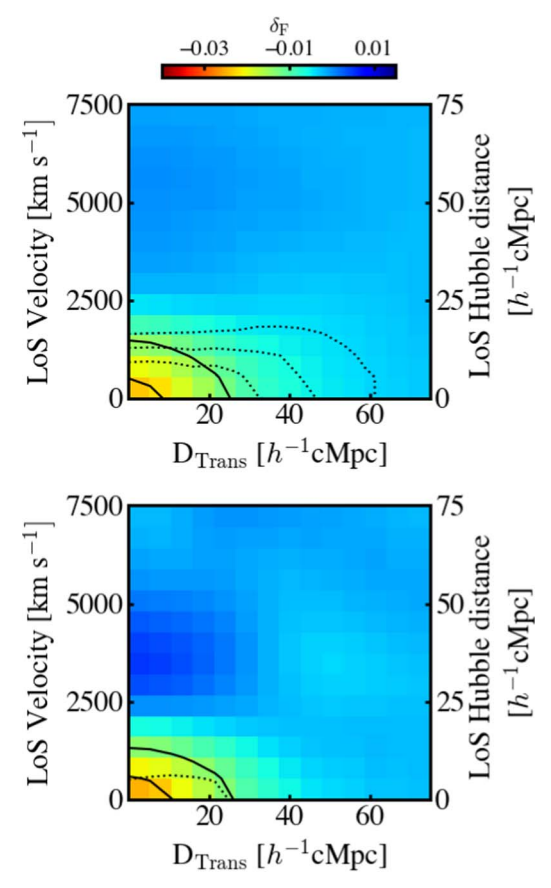
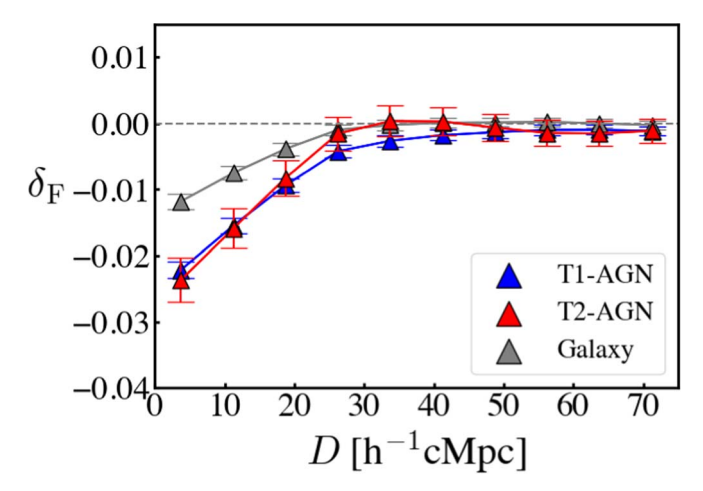


Figure 19. Same as Figure 7, but for the T1-AGN (top figure) and T2-AGN (bottom figure) subsamples.



**Figure 20.** Same as Figure 11, but for the T1-AGN (blue) and T2-AGN (red) subsamples and the galaxy (gray) sample.

peak values of the LOS and transverse H I radial profiles suggest that the selectively different orientation and opening angles of the dusty tori of the type 1 and type 2 AGNs do not significantly affect the Ly $\alpha$  forest absorption at the scale  $\lesssim 15~h^{-1}$  cMpc, or our measurement does not have enough sensitivity to detect the difference of Ly $\alpha$  forest absorption between type 1 and type 2 AGNs.

For the H I radial profiles at the scale >15  $h^{-1}$  cMpc, we find that the  $\delta_F$  value for the LOS H I radial profile of the T1-AGN subsample is smaller than those of the T2-AGN subsample over the  $1\sigma$  error bar at the scale around 25  $h^{-1}$  cMpc. This

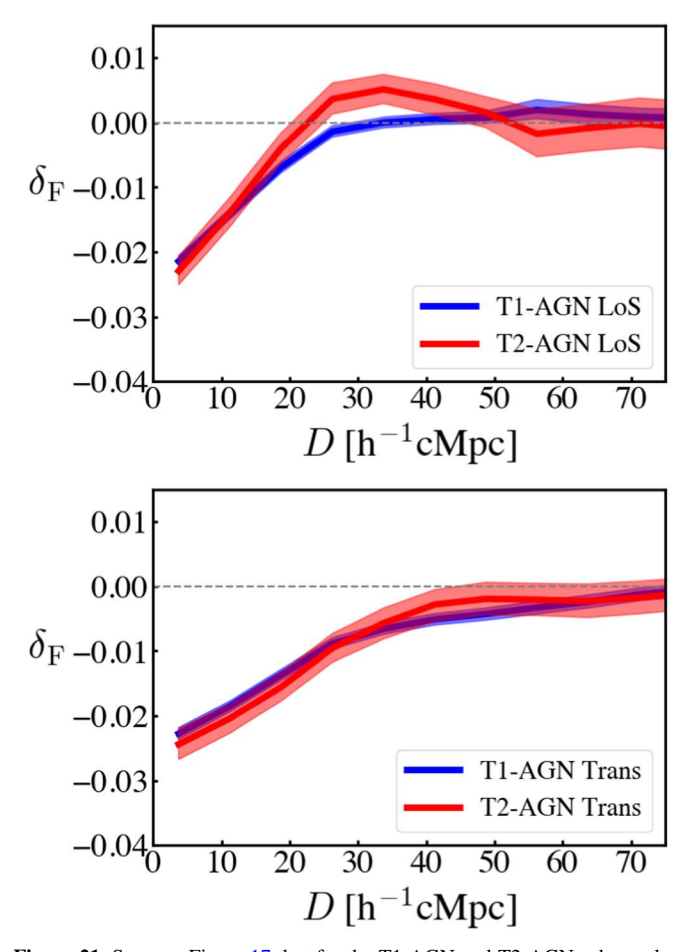


Figure 21. Same as Figure 17, but for the T1-AGN and T2-AGN subsamples.

result may hint that the type 2 AGNs have a stronger power of ionization at 25  $h^{-1}$  cMpc than the type 1 AGNs. The interpretation of ionization at large scales is in Section 5.5.

# 5.4. Average HI Profiles around Galaxy

We derive the 2D H I profile at the positions of the galaxy sample sources in the same manner as that of the All-AGN sample sources. Figure 22 presents the 2D H I profile of the galaxy sample sources. There is a clear  $10.5\sigma$  detection at the source position of (0,0). Similarly, we calculate the H I radial profile from the 2D H I profile of the galaxy sample (Figure 23). The H I radial profile of the galaxy sample shows a trend similar to those of the All-AGN sample. For both the galaxy and All-AGN samples, the H I radial profile decreases toward the large scales, reaching cosmic average.

In Figure 22, we find that the Ly $\alpha$  forest absorptions in the LOS and transverse directions are different. A similar difference between the values of  $A_F$  in LOS and transverse directions of 2D H I profiles is claimed by Mukae et al. (2020). To investigate the difference between the Ly $\alpha$  forest absorptions in LOS and transverse directions for the galaxy sample, we present the LOS and transverse H I radial profiles of the galaxy sample in Figure 25. We find that the LOS and transverse H I radial profiles of the galaxy sample show different gradients of the increasing  $\delta_F$  at the scale  $D \sim 3.75$ –50  $h^{-1}$  cMpc. This difference can be explained by the gas version of the Kaiser effect that we discussed in Section 5.2. In the LOS H I radial profile of the galaxy sample, we find that the  $\delta_F$  values are

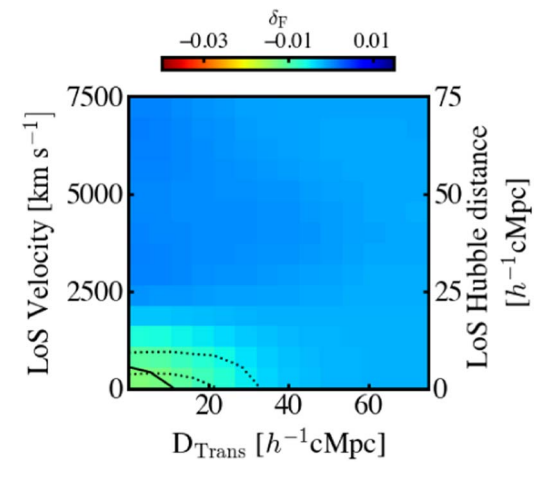


**Figure 22.** 2D H I profile of the galaxy sample sources. The color map indicates the  $\delta_F$  values of each cell of the 2D H I profile. The dotted lines show confidence level contours of  $3\sigma$  and  $6\sigma$ . The solid line presents the contour where  $\delta_F=-0.01$ .

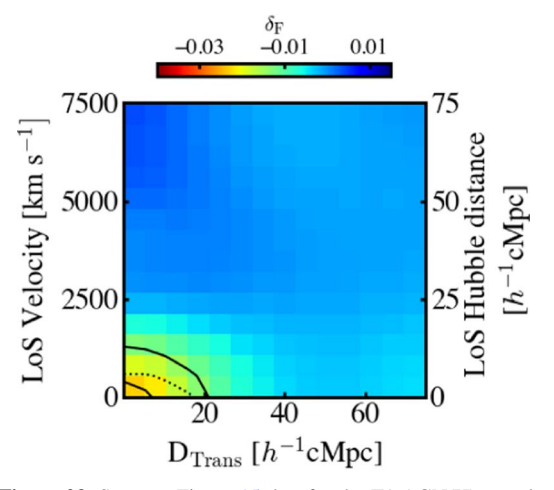


Figure 23. Same as Figure 15, but for the T1-AGN(H) sample.

positive on the scale of D=25–70  $h^{-1}$  cMpc, which is similar to the positive  $\delta_F$  values we found on the large scale of the LOS H I radial profile for the All-AGN sample. We discuss these positive  $\delta_F$  values on the LOS H I radial profile of the galaxy sample in Section 5.5.

# 5.4.1. Galaxy-AGN Dependence

We derive 2D H I profiles for the T1-AGN(H) sample constructed from the HETDEX data. Figures 22 and 23 show the 2D H I profiles of the galaxy and T1-AGN(H) samples, respectively. We find  $7.6\sigma$  detection around the source position for the T1-AGN(H) sample. Figure 24 presents the H I radial profiles of the galaxy and T1-AGN(H) samples derived from the 2D H I profiles. We also compare the H I radial profiles of the galaxy sample with those of T1-AGN and T2-AGN in Figure 20. In the H I radial profiles of the galaxy and T1-AGN (H) samples, the  $\delta_F$  values decrease toward the source position D=0. In Figure 24 (Figure 20), we find that the  $\delta_F$  values of T1-AGN(H) (T1-AGN and T2-AGN) are smaller than those of the galaxies at  $\lesssim 20~h^{-1}$  cMpc. These  $\delta_F$  excesses of the AGN may be explained by the hosting dark matter halos of the AGNs

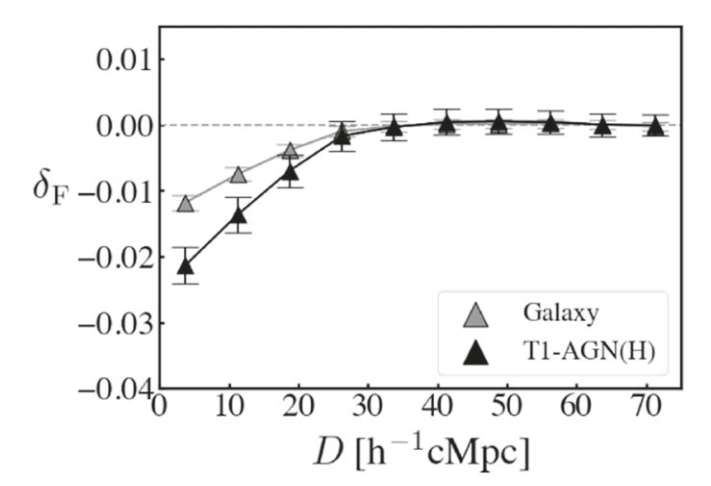


Figure 24. Same as Figure 16, but for galaxy (gray) and T1-AGN(H) (black) samples.

being more massive than those of the galaxies. Momose et al. (2021) also investigate the H I radial profile around AGNs and find Ly $\alpha$  forest absorption decrement at the source center ( $\lesssim 5 h^{-1}$  Mpc). They argue that this trend can be explained by the proximity effect. On the other hand, their result is different from ours that the  $A_F$  values monotonically increase with decreasing distance. This difference between our results and those of Momose et al. is produced by the fact that our results for  $\lesssim 10 h^{-1}$  cMpc are largely affected by the Ly $\alpha$  transmission fluctuation at  $\sim 10 h^{-1}$  cMpc due to the coarse resolution of our H I tomography map,  $15 h^{-1}$  cMpc, in contrast with  $2.5 h^{-1}$  cMpc for the resolution of Momose et al. (2021).

We then derive the LOS and transverse radial H I profiles of the T1-AGN(H) sample. The results of the profiles are shown in Figure 25. Similar to the LOS and transverse H I radial profiles of the All-AGN and galaxy samples, the gas version of the Kaiser effect and the positive  $\delta_F$  in the LOS direction on the scale beyond  $D=25~h^{-1}$  cMpc are also found in those of the T1-AGN(H) sample.

#### 5.5. Comparison with Theoretical Models

There are theoretical models of H I radial profiles around AGNs that are made by Font-Ribera et al. (2013). Font-Ribera et al. (2013) present their H I radial profiles with the LOS distance in the form of the CCF.

We first calculate theoretical CCFs of All-AGN, following the definition of the CCF presented in Font-Ribera et al. (2012, 2013). Font-Ribera et al. (2013) assume the linear cross-power spectrum of the QSOs and  $Ly\alpha$  forest,

$$P_{qF}(\mathbf{k}, z) = b_q(z)[1 + \beta_q(z)\mu_k^2]b_F(z)[1 + \beta_F(z)\mu_k^2]P_L(\mathbf{k}, z),$$
(10)

where  $P_L(k, z)$  is the linear matter power spectrum. Here  $\mu_k$  is the cosine of the angle between the Fourier mode and the LOS (Kaiser 1987). The values of  $b_q$  and  $b_F$  ( $\beta_q$  and  $\beta_F$ ) are the bias factors (redshift space distortion parameters) of the QSO and Ly $\alpha$  density, respectively.

The redshift distortion parameter of QSO obeys the relation  $\beta_q = f(\Omega)/b_q$ , where  $f(\Omega)$  is the logarithmic derivative of the linear growth factor (Kaiser 1987),  $b_q = 3.8 \pm 0.3$  (White et al. 2012). We use the condition of Ly $\alpha$  forest,  $b_F(1+\beta_F) = -0.336$  for  $b_F \propto (1+z)^{2.9}$ , that is determined

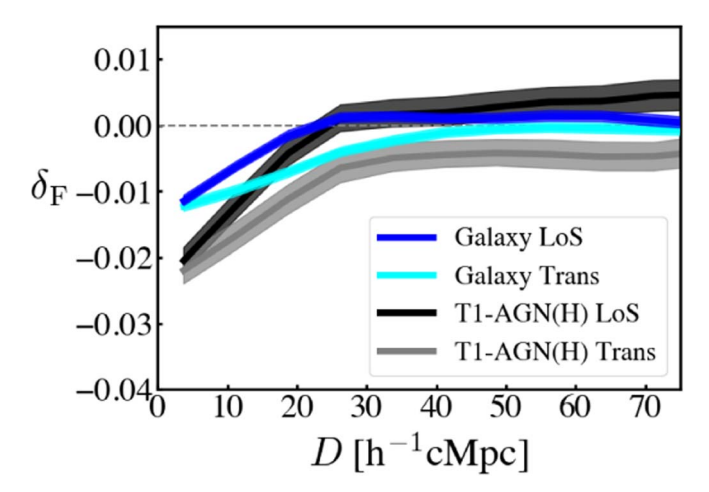


Figure 25. Same as Figure 13, but for the galaxy and T1-AGN(H) samples.

by observations of Ly $\alpha$  forest at  $z \simeq 2.25$  (Slosar et al. 2011). Font-Ribera et al. (2013) estimate the CCF of QSOs by the Fourier transform of  $P_{qF}$  (Hamilton 1992):

$$\xi(\mathbf{r}) = \xi_0(r)P_0(\mu) + \xi_2(r)P_2(\mu) + \xi_4(r)P_4(\mu), \tag{11}$$

where  $\mu$  is the cosine of angle between the position r and the LOS in the redshift space. The values of  $P_0$ ,  $P_2$ , and  $P_4$  are the Legendre polynomials,  $P_0 = 1$ ,  $P_2 = (3\mu^2 - 1)$ , and  $P_4 = (35\mu^4 - 30\mu^2 + 3)/8$ , respectively. The functions of  $\xi_0$ ,  $\xi_2$ , and  $\xi_4$  are

$$\xi_0(r) = b_q b_F [1 + (\beta_q + \beta_F)/3 + \beta_q \beta_F/5] \zeta(r),$$
 (12)

$$\xi_2(r) = b_q b_F [2/3(\beta_q + \beta_F) + 4/7\beta_q \beta_F] [\zeta(r) - \overline{\zeta}(r)],$$
(13)

$$\xi_4(r) = 8/35b_q b_F \beta_q \beta_F [\zeta(r) - 5/2\overline{\zeta}(r) - 7/2\overline{\overline{\zeta}}(r)]. \quad (14)$$

The function  $\zeta(r)$  is the standard cold dark matter linear correlation function in real space (Bardeen et al. 1986; Hamilton et al. 1991). The functions  $\bar{\zeta}(r)$  and  $\bar{\bar{\zeta}}(r)$  are given by

$$\bar{\zeta}(r) \equiv 3r^{-3} \int_0^r \zeta(s) s^2 ds,\tag{15}$$

$$\bar{\zeta}(r) \equiv 5r^{-5} \int_0^r \zeta(s) s^4 ds. \tag{16}$$

In Figure 26, we present  $D\xi$  as a function of the LOS distance for the model of Font-Ribera et al. (2013) that is calculated under the assumption of the mean overdensity of the 15  $h^{-1}$  cMpc corresponding to the spatial resolution of our observational results.

To compare our observational measurements with the model CCF of Font-Ribera et al. (2013), we calculate the value of  $\xi$  for our All-AGN sample. The value of  $\xi$  in each cell  $\xi_{\text{cell}}$  is calculated by

$$\xi_{\text{cell}} = \frac{\sum_{i \in \text{cell}} \omega_i \delta_{Fi}}{\sum_{i \in \text{cell}} \omega_i},$$
(17)

where  $\omega_i$  is the weight determined by the observational errors and the intrinsic variance of the Ly $\alpha$  forest. Note that the  $\delta_{Fi}$  used in Font-Ribera et al. (2012, 2013) is the raw  $\delta_{Fi}$ , which is not undergoing the Wiener filtering scheme. The value of  $\omega_i$  is

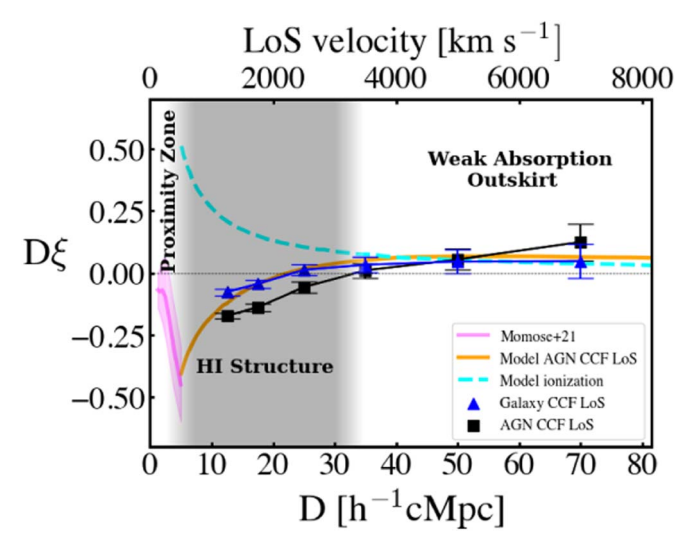


**Figure 26.** Comparison between our All-AGN and galaxy results and the models of Font-Ribera et al. (2013) in the LOS CCF  $\xi$  multiplied by distance (D). The black and blue symbols are the results derived from the All-AGN and galaxy samples sources, respectively. The orange curve is the LOS CCF of QSOs with the Ly $\alpha$  forest derived by Font-Ribera et al. (2013). The cyan dashed curve shows the ionization of radiation effect taken from Font-Ribera et al. (2013). The pink line presents the CCF of AGNs obtained by Momose et al. (2021). The gray shade presents the range of the H I structure. Two white areas show the regions of proximity zone and weak absorption outskirts. The horizontal gray line indicates the cosmic average where  $D\xi = 0$ .

obtained by

$$\omega_i = \left[ \sigma_F^2(z_i) + \frac{1}{\langle S/N \rangle^2 \times \langle F(z_i) \rangle^2} \right]^{-1}, \tag{18}$$

where  $\sigma_F(z_i)$  is the intrinsic variance of the Ly $\alpha$  forest. The value of  $\langle F(z_i) \rangle$  is the cosmic average Ly $\alpha$  transmission (Equation (4)). We adopt  $\langle S/N \rangle = 1.4$ , which is the criterion of the background source selection (Section 3.3). The intrinsic variance,  $\sigma_F(z_i)$ , of the Ly $\alpha$  forest taken from Font-Ribera et al. (2013) is

$$\sigma_F^2(z_i) = 0.065[(1+z_i)/3.25]^{3.8}. (19)$$

We calculate  $\xi$  with our All-AGN sample via Equations (17), (18), and (19), using binning sizes the same as those in Font-Ribera et al. (2013). We present  $\xi$  multiplied by D with the black squares in Figure 26. For reference, we also derive the  $\xi$  for our galaxy sample shown by the blue triangles.

In Figure 26, we find that the  $D\xi$  profile of our All-AGN sample shows a trend similar to that of the model predicted by Font-Ribera et al. (2013). The observational  $D\xi$  profile of our All-AGN sample shows a good agreement with the model  $D\xi$ profile of Font-Ribera et al. (2013) at the scale of  $D > 30 h^{-1}$ cMpc. Equation (10) of the linear theory model already includes the parameter of redshift distortion,  $\beta$ , which is due to the coherent motions of the HI gas around the quasars. The model is a prediction on the impact of the clustering effect that a quasar statistically gathers HI gas from large scales, even  $\gtrsim$ 30  $h^{-1}$  cMpc. The positive  $D\xi$  structure  $\gtrsim$ 30  $h^{-1}$  cMpc can be explained by "cosmic voids" like structure whose H I gas column density is slightly smaller than the cosmic average. Though the general trend of the positive  $D\xi$  structure of our results at  $\gtrsim 30 \ h^{-1}$  cMpc is the same as the model  $D\xi$  profile, the model  $D\xi$  profile is slightly lower than the  $D\xi$  profiles of the observations at  $\geq 60 \ h^{-1}$  cMpc. We cannot rule out the

possibility that the ionization of AGNs contributes to further reduction in the Ly\$\alpha\$ absorption at \$\geq 60 \ h^{-1}\$ cMpc. Font-Ribera et al. (2013) also present the model of ionization. In the model of ionization, Font-Ribera et al. (2013) assume the spectrum of the AGN at D=0 with  $L_{\nu} \propto \nu^{-\alpha}$ , where  $\alpha=1.5$  (1.0) for the frequency  $\nu$  over (below) the Lyman limit. The luminosity of  $\lambda=1420$  Å is normalized as  $L_{\nu}=3.1\times10^{30}$  erg s<sup>-1</sup> Hz<sup>-1</sup>, which is taken from the mean luminosity of the SDSS data release 9 quasars. No assumptions of AGN type have been made in the models of Font-Ribera+13. Based on the model of ionization, Font-Ribera et al. (2013) calculate  $\xi$  for the homogeneous gas radiated by AGNs and obtain the function

$$\xi = 0.0065(20 \, h^{-1} \text{cMpc}/D)^2.$$
 (20)

With the  $\xi$  function, we calculate  $D\xi$ , which is presented with the cyan dashed curve in Figure 26. The cyan dashed curve shows the plateau at  $D \ge 40 h^{-1}$  cMpc with positive  $D\xi$  values. To distinguish the large-scale positive  $D\xi$  values, which are referred to as the "weak absorption outskirts," from the proximity zone created by the proximity effect, we plot the observational CCF of AGNs obtained by Momose et al. (2021) in Figure 26. The AGN CCF obtained by Momose et al. shows a decreasing Ly $\alpha$  forest absorption toward source position  $(D = 0 h^{-1} \text{ cMpc})$  caused by the proximity effect. If the weak absorption outskirts are created by the combination of the clustering effect and ionization, our findings indicate that the H I radial profile of AGNs may have transitions from proximity zones ( $\leq$ a few  $h^{-1}$  cMpc) to the H I structures ( $\sim$ 1–30  $h^{-1}$ cMpc) and the ionized outskirts ( $\gtrsim 30 \ h^{-1}$  cMpc). The hard radiation may pass through the H I structure owing to the small cross section and ionize the HI gas in the regions of ionized outskirts. Because of the low recombination rate, the HI gas remains ionized in the weak absorption outskirts.

Figure 26 shows that the  $D\xi$  values in the range of H I structure around AGNs and galaxies are also similar. Interestingly, the  $D\xi$  profile of our galaxy sample also shows positive  $D\xi$  values toward  $\gtrsim 30~h^{-1}$  cMpc, which is similar to those of the AGN model and our All-AGN sample. This result may suggest that the H I gas at large scale ( $\gtrsim 20~h^{-1}$  cMpc) around galaxies also falls toward the source position (D=0). Regions around galaxies are special, as galaxies are clustered together. Galaxies in this work are bright with  $M_{\rm UV} < -22$  mag. The galaxies can be hosted by massive halos and are likely to distribute at overdensity regions. The overdensity region suggests that each galaxy can be surrounded by several galaxies. Although it is difficult for a galaxy to trigger the clustering effect for the H I gas on a scale of  $\gtrsim 20~h^{-1}$  cMpc, a group of galaxies may have enough gravitational power to aggregate the H I on this scale.

#### 6. Summary

We reconstruct two 3D H I tomography maps based on the Ly $\alpha$  forests in the spectra of 14,763 background QSOs from SDSS with no signatures of the damped Ly $\alpha$  system or BALs. The maps cover the extended Fall and Spring fields defined by the HETDEX survey. The spatial volumes of the reconstructed 3D H I tomography maps are  $2257 \times 233 \times 811 \ h^{-3} \ \text{cMpc}^3$  and  $3475 \times 1058 \times 811 \ h^{-3} \ \text{cMpc}^3$ . We investigate Ly $\alpha$  forest absorption around galaxies and AGNs with samples made from

HETDEX and SDSS results in our study field. Our results are summarized below.

- 1. We derive the 2D H I and H I radial profiles of the All-AGN sample consisting of SDSS AGNs. We find that the 2D H I profile is more extended in the transverse direction than along the LOS. In the H I radial profile All-AGN sample, the values of Ly $\alpha$  transmission fluctuation,  $\delta_F$ , increase toward the large scale, touching to  $\delta_F \sim 0$ .
- We compare the H I radial profiles derived from the T1-AGN and T1-AGN(H) subsamples, whose L<sub>1350</sub> distributions are the same. We find that the H I radial profile of the T1-AGN subsample agrees with that of the T1-AGN (H) subsample. This agreement suggests that the systematic uncertainty between the SDSS and HETDEX results is negligible.
- 3. We examine the dependence of the H I profile on AGN luminosity by deriving the 2D H I, H I radial, LOS H I radial, and transverse H I radial profiles of the All-AGN-L3 (the faintest), All-AGN-L2, and All-AGN-L1 (the brightest) subsamples. We find that the Lyα forest absorption is the greatest in the lowest-luminosity AGN subsample and that the Lyα forest absorption becomes weaker with increasing AGN luminosity. This result suggests that, on average, if the density of H I gas around bright AGN is greater than (or comparable to) that of faint AGNs, the ionization fraction of H I gas around bright AGNs is higher than that around faint AGNs.
- 4. We investigate the AGN type dependence of Ly $\alpha$  forest absorption around type 1 and type 2 AGNs by the 2D H I, H I radial, LOS H I radial, and transverse H I radial profiles extracted from the T1-AGN and T2-AGN subsamples with the same  $L_{1350}^{\rm spec}$  distributions. The comparison between the H I radial profiles of T1-AGN and T2-AGN subsamples indicates that the Ly $\alpha$  transmission fluctuation around the T2-AGN subsample is comparable to that of the T1-AGN subsample on average. This trend suggests that the selectively different opening angle and orientation of the dusty torus for type 1 and type 2 AGNs do not have a significant impact on the megaparsec-scale Ly $\alpha$  forest absorption, or the sensitivity of our result is not enough to detect the difference.
- 5. We compare the Ly $\alpha$  forest absorptions around galaxies and type 1 AGNs with the 2D HI, HI radial, LOS HI radial, and transverse HI radial profiles derived from the galaxy and T1-AGN(H) sample sources. The Ly $\alpha$  transmission fluctuation values,  $\delta_F$ , around the T1-AGN (H) sample are larger than those of the galaxy sample on average. This result may be caused by the dark matter halos of type 1 AGNs having a larger mass than the one of galaxies on average.
- 6. We find that the H I radial profiles of the LOS distance for the galaxy and All-AGN samples show positive  $\delta_F$  values, which means weak Ly $\alpha$  forest absorption, at the scale over  $\sim 30~h^{-1}$  cMpc. We extract the  $D\xi$  profile of our galaxy and All-AGN samples to compare with the model CCF of AGNs from Font-Ribera et al. (2013). The general trend of the positive  $D\xi$  at  $\gtrsim 30~h^{-1}$  cMpc is the same as the model CCF. This results suggest that the H I radial profile of AGNs has transitions from proximity zones ( $\lesssim$ a few  $h^{-1}$  cMpc) to the H I rich structures

 $(\sim 1 - 30 \ h^{-1} \ \text{cMpc})$  and the weak absorption outskirts  $(\gtrsim 30 \ h^{-1} \ \text{cMpc})$ .

#### Acknowledgments

We thank Nobunari Kashikawa, Khee-Gan Lee, Akio Inoue, Rikako Ishimoto, Shengli Tang, Yongming Liang, Rieko Momose, and Koki Kakiichi for giving us helpful comments.

HETDEX is led by the University of Texas at Austin McDonald Observatory and Department of Astronomy with from the Ludwig-Maximilians-Universität participation München, Max-Planck-Institut für Extraterrestrische Physik (MPE), Leibniz-Institut für Astrophysik Potsdam (AIP), Texas A&M University, Pennsylvania State University, Institut für Astrophysik Göttingen, The University of Oxford, Max-Planck-Institut für Astrophysik (MPA), The University of Tokyo, and Missouri University of Science and Technology. In addition to Institutional support, HETDEX is funded by the National Science Foundation (grant AST-0926815), the State of Texas, the US Air Force (AFRL FA9451-04-2-0355), and generous support from private individuals and foundations. The observations were obtained with the Hobby-Eberly Telescope (HET), which is a joint project of the University of Texas at Austin, the Pennsylvania State University, Ludwig-Maximilians-Universität München, and Georg-August-Universität Göttingen. The HET is named in honor of its principal benefactors, William P. Hobby and Robert E. Eberly. The authors acknowledge the Texas Advanced Computing Center (TACC) at The University of Texas at Austin for providing high-performance computing, visualization, and storage resources that have contributed to the research results reported within this paper. URL:http://www.tacc.utexas.edu.

VIRUS is a joint project of the University of Texas at Austin, Leibniz-Institut für Astrophysik Potsdam (AIP), Texas A&M University (TAMU), Max-Planck-Institut für Extraterrestrische Physik (MPE), Ludwig-Maximilians-Universität Muenchen, Pennsylvania State University, Institut für Astrophysik Göttingen, University of Oxford, and the Max-Planck-Institut für Astrophysik (MPA). In addition to Institutional support, VIRUS was partially funded by the National Science Foundation, the state of Texas, and generous support from private individuals and foundations.

This work is supported in part by MEXT/JSPS KAKENHI grant No. 21H04489 (HY), JST FOREST Program, grant No. JP-MJFR202Z (HY).

K.M. acknowledges financial support from the Japan Society for the Promotion of Science (JSPS) through KAKENHI grant No. 20K14516.

This paper is supported by World Premier International Research Center Initiative (WPI Initiative), MEXT, Japan, the joint research program of the Institute of Cosmic Ray Research (ICRR), the University of Tokyo, and KAKENHI (19H00697, 20H00180, and 21H04467) Grant-in-Aid for Scientific Research (A) through the Japan Society for the Promotion of Science.

#### **Appendix**

In the Appendix, we include the sky distribution of all foreground and background sources discussed in Section 3 that were not previously presented (Figures 27–30).

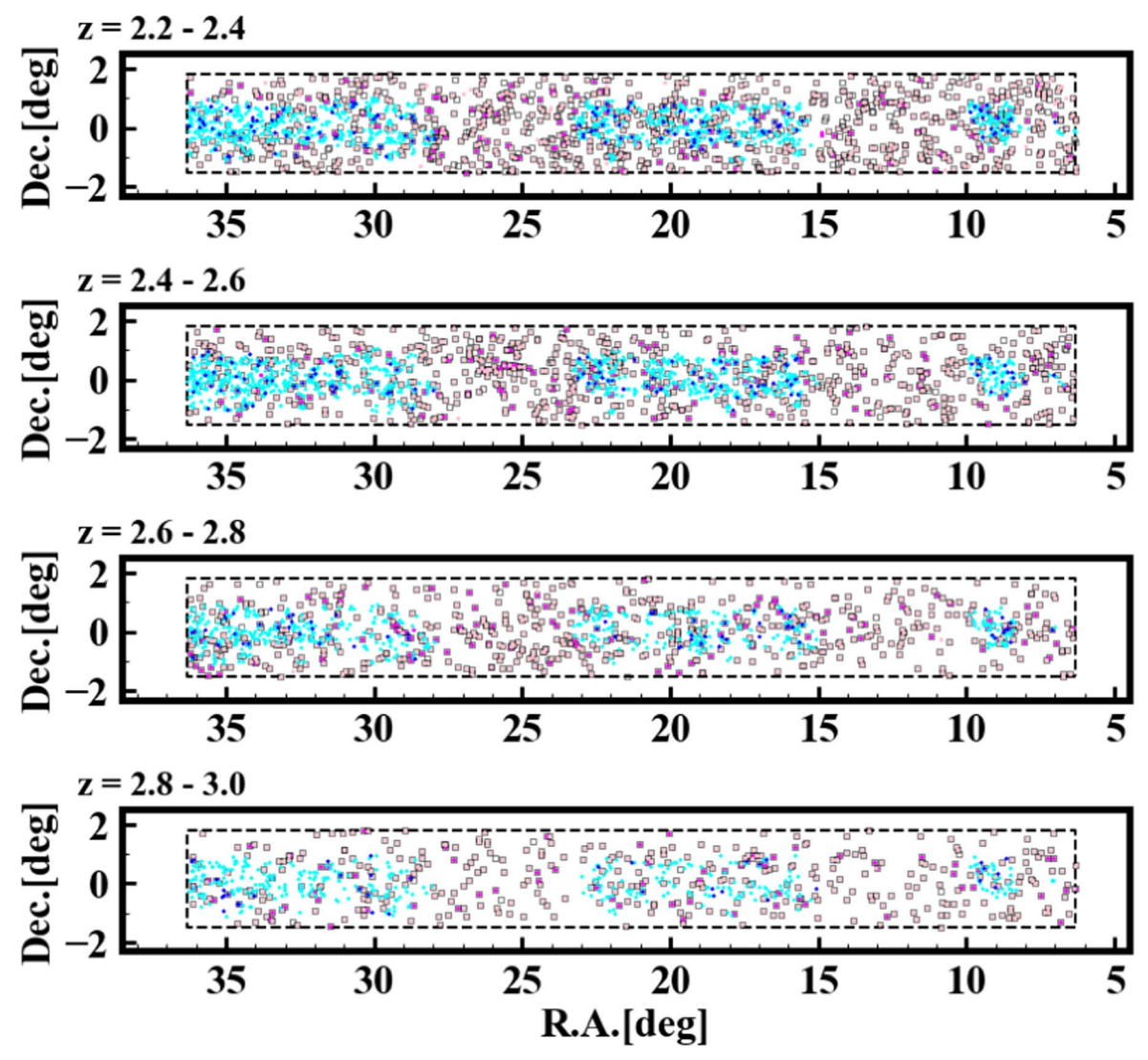


Figure 27. Continued from Figure 1. The different panels denote the coverages over different redshift ranges shown at the top left of each panel.

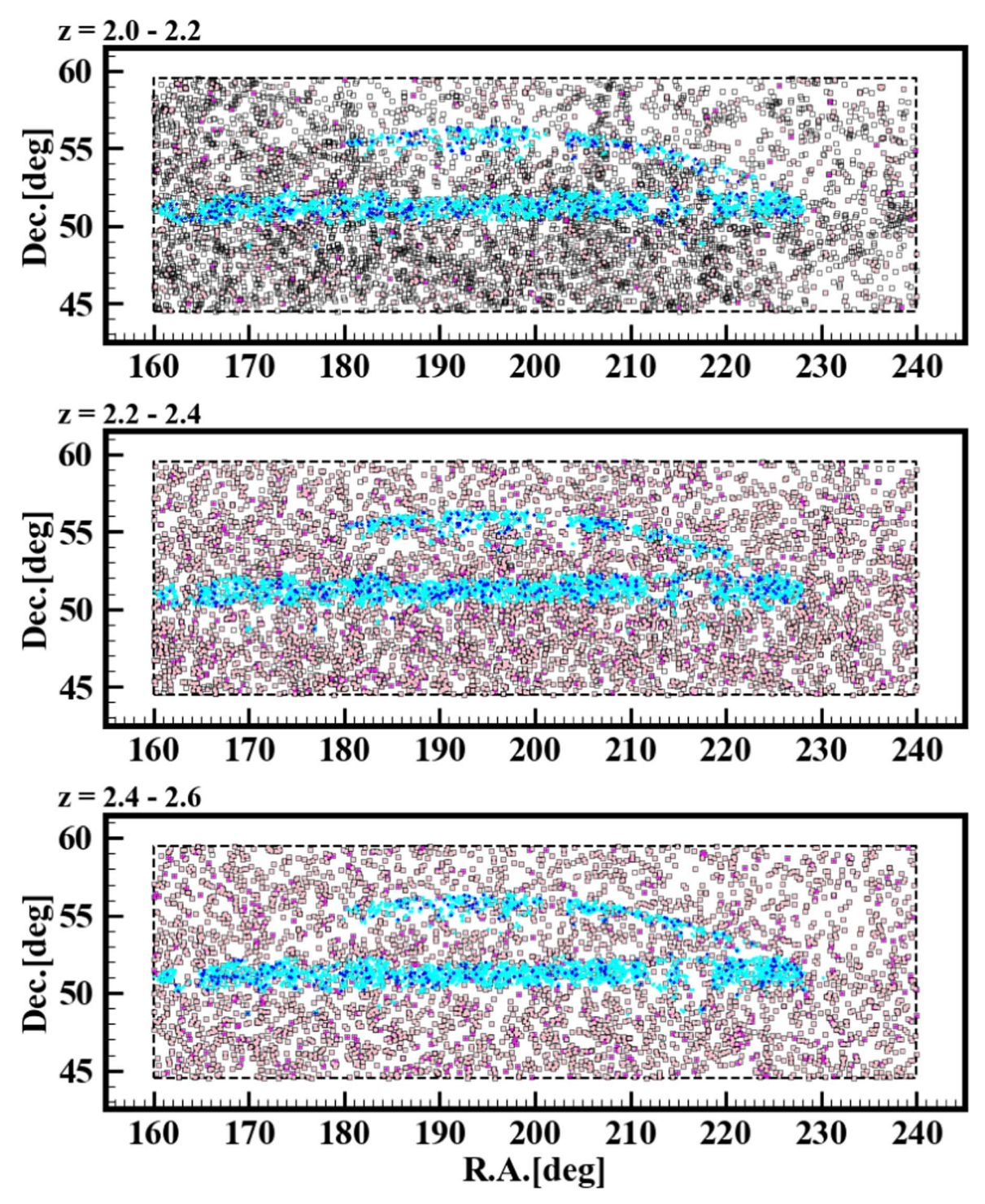


Figure 28. Same as Figure 1, but for the foreground sources in the ExSpring field.

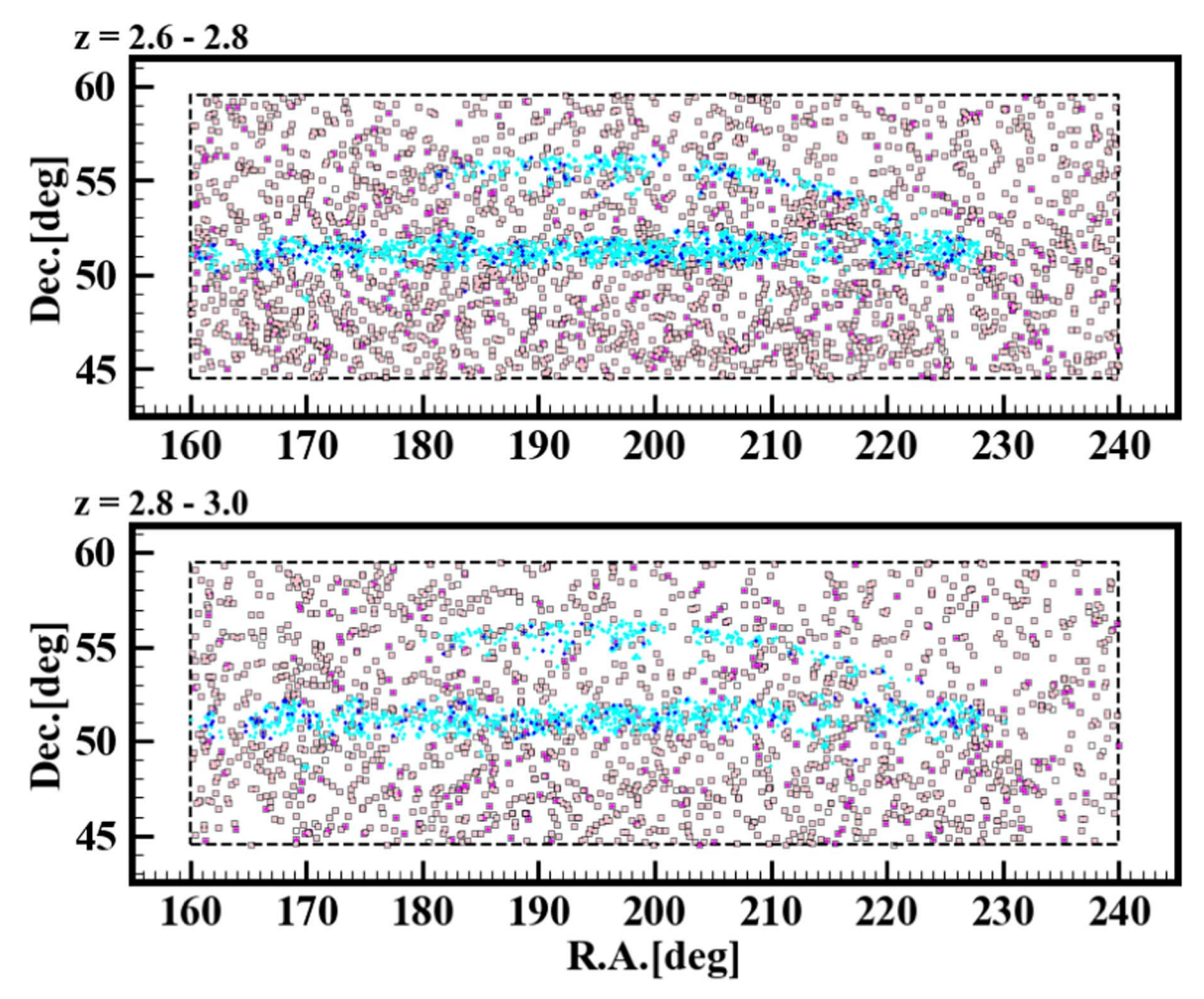


Figure 29. Continued from Figure 28.

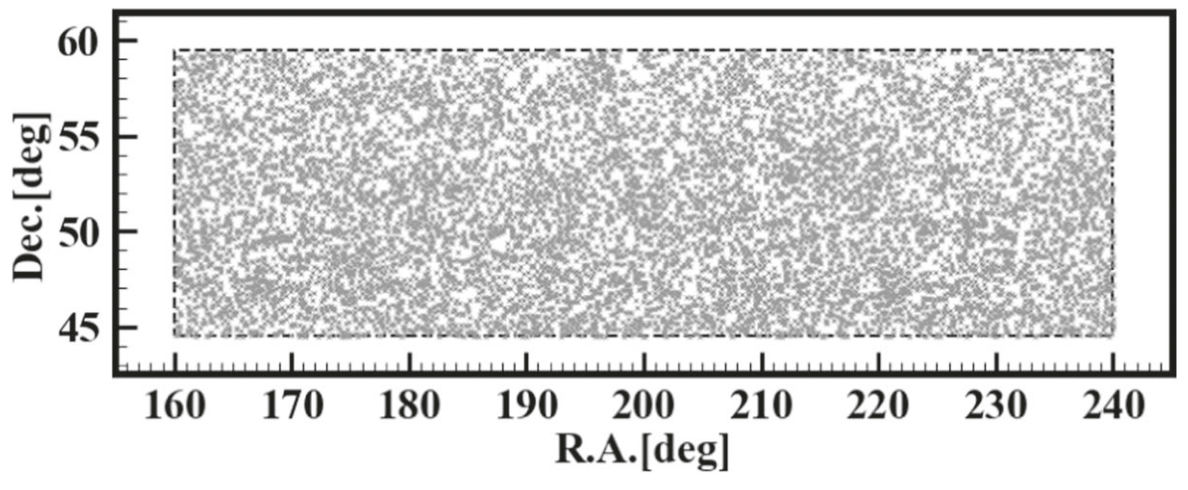


Figure 30. Same as Figure 2, but for the background sources in the ExSpring field.

# **ORCID iDs**

 Erin Mentuch Cooper https://orcid.org/0000-0002-2307-0146

Dustin Davis https://orcid.org/0000-0002-8925-9769

Daniel J. Farrow https://orcid.org/0000-0003-2575-0652

Karl Gebhardt https://orcid.org/0000-0002-8433-8185

Gary J. Hill https://orcid.org/0000-0001-6717-7685

Chenxu Liu https://orcid.org/0000-0001-5561-2010

Donald P. Schneider https://orcid.org/0000-0001-7240-7449

#### References

```
Adelberger, K. L., Shapley, A. E., Steidel, C. C., et al. 2005, ApJ, 629, 636
Adelberger, K. L., Steidel, C. C., Shapley, A. E., & Pettini, M. 2003, ApJ,
   584, 45
Aihara, H., Arimoto, N., Armstrong, R., et al. 2018, PASJ, 70, S4
Alexandroff, R., Strauss, M. A., Greene, J. E., et al. 2013, MNRAS, 435, 3306
Antonucci, R. R. J., & Miller, J. S. 1985, ApJ, 297, 621
Bardeen, J. M., Bond, J. R., Kaiser, N., & Szalay, A. S. 1986, ApJ, 304, 15
Bosch, J., Armstrong, R., Bickerton, S., et al. 2018, PASJ, 70, S5
Bovy, J., Myers, A. D., Hennawi, J. F., et al. 2012, ApJ, 749, 41
Caucci, S., Colombi, S., Pichon, C., et al. 2008, MNRAS, 386, 211
Chabanier, S., Etourneau, T., Le Goff, J.-M., et al. 2022, ApJS, 258, 18
Cooper, E. M., Gebhardt, K., Davis, D., et al. 2023, ApJ, 943, 177
Crighton, N. H. M., Bielby, R., Shanks, T., et al. 2011, MNRAS, 414, 28
Davis, D., Gebhardt, K., Cooper, E. M., et al. 2023, ApJ, 946, 86
Davis, D., Gebhardt, K., Mentuch Cooper, E., et al. 2021, ApJ, 920, 122
Dawson, K. S., Kneib, J.-P., Percival, W. J., et al. 2016, AJ, 151, 44
D'Odorico, V., Bruscoli, M., Saitta, F., et al. 2008, MNRAS, 389, 1727
Draine, B. T. 2011, Physics of the Interstellar and Intergalactic Medium
   (Princeton, NJ: Princeton Univ. Press)
Faucher-Giguère, C.-A., Lidz, A., Hernquist, L., & Zaldarriaga, M. 2008a,
   ApJL, 682, L9
Faucher-Giguère, C.-A., Lidz, A., Zaldarriaga, M., & Hernquist, L. 2008b,
    pJ, 673, 39
Faucher-Giguère, C.-A., Prochaska, J. X., Lidz, A., Hernquist, L., &
   Zaldarriaga, M. 2008c, ApJ, 681, 831
Font-Ribera, A., Arnau, E., Miralda-Escudé, J., et al. 2013, JCAP, 2013, 018
Font-Ribera, A., Miralda-Escudé, J., Arnau, E., et al. 2012, JCAP, 2012, 059
Fox, A. 2017, in Gas Accretion onto Galaxies, ed. A. Fox & M. Davé, Vol. 430
  (Berlin: Springer)
Gebhardt, K., Mentuch Cooper, E., Ciardullo, R., et al. 2021, ApJ, 923, 217
Gronwall, C., Ciardullo, R., Hickey, T., et al. 2007, ApJ, 667, 79
Gunn, J. E., Siegmund, W. A., Mannery, E. J., et al. 2006, AJ, 131, 2332
Hamilton, A. J. S. 1992, ApJL, 385, L5
Hamilton, A. J. S., Kumar, P., Lu, E., & Matthews, A. 1991, ApJL, 374, L1
Hill, G. J., Kelz, A., Lee, H., et al. 2018, Proc. SPIE, 10702, 107021K
Hill, G. J., Lee, H., MacQueen, P. J., et al. 2021, AJ, 162, 298
                    NRAS, 227, 1
Kaiser, N. 1987, M
Kelz, A., Jahn, T., Haynes, D., et al. 2014, Proc. SPIE, 9147, 914775
Konno, A., Ouchi, M., Nakajima, K., et al. 2016, ApJ, 823, 20
Krolewski, A., Lee, K.-G., White, M., et al. 2018, ApJ, 861, 60
```

Lee, K.-G., Hennawi, J. F., Stark, C., et al. 2014, ApJL, 795, L12

Lee, K.-G., Hennawi, J. F., White, M., et al. 2016, ApJ, 817, 160 Lee, K.-G., Krolewski, A., White, M., et al. 2018, ApJS, 237, 31

Lee, K.-G., Suzuki, N., & Spergel, D. N. 2012, AJ, 143, 51

```
Lyke, B. W., Higley, A. N., McLane, J. N., et al. 2020, ApJS, 250, 8
Mawatari, K., Inoue, A. K., Kousai, K., et al. 2016, ApJ, 817, 161
Meiksin, A. A. 2009, RvMP, 81, 1405
Mo, H., van den Bosch, F. C., & White, S. 2010, Galaxy Formation and
  Evolution (Cambridge: Cambridge Univ. Press)
Momose, R., Shimasaku, K., Kashikawa, N., et al. 2021, ApJ, 909, 117
Mukae, S., Ouchi, M., Hill, G. J., et al. 2020, ApJ, 903, 24
National Academies of Sciences, Engineering, and Medicine 2021, Pathways
   to Discovery in Astronomy and Astrophysics for the 2020s (Washington,
   DC: The National Academies Press)
Panessa, F., & Bassani, L. 2002, A&A, 394, 435
Pâris, I., Petitjean, P., Aubourg, É., et al. 2018, A&A, 613, A51
Pâris, I., Petitjean, P., Rollinde, E., et al. 2011, A&A, 530, A50
Pichon, C., Vergely, J. L., Rollinde, E., Colombi, S., & Petitjean, P. 2001,
   MNRAS, 326, 597
Prochaska, J. X., Hennawi, J. F., Lee, K.-G., et al. 2013, ApJ, 776, 136
Rakic, O., Schaye, J., Steidel, C. C., & Rudie, G. C. 2012, ApJ, 751, 94
Rakshit, S., Stalin, C. S., & Kotilainen, J. 2020, ApJS, 249, 17
Ramsey, L. W., Sebring, T. A., & Sneden, C. A. 1994, Proc. SPIE, 2199, 31
Rauch, M. 1998, ARA&A, 36, 267
Ravoux, C., Armengaud, E., Walther, M., et al. 2020, JCAP, 2020, 010
Rudie, G. C., Steidel, C. C., Trainor, R. F., et al. 2012, ApJ, 750, 67
Slosar, A., Font-Ribera, A., Pieri, M. M., et al. 2011, JCAP, 2011, 001
Smee, S. A., Gunn, J. E., Uomoto, A., et al. 2013, AJ, 146, 32
Spinoglio, L., & Fernández-Ontiveros, J. A. 2021, in IAU Symp. 356, Nuclear
   Activity in Galaxies Across Cosmic Time, ed. M. Pović et al. (Cambridge:
   Cambridge Univ. Press), 29
Stark, C. W., Font-Ribera, A., White, M., & Lee, K.-G. 2015, MNRAS,
   453, 4311
Steidel, C. C., Erb, D. K., Shapley, A. E., et al. 2010, ApJ, 717, 289
Suzuki, N., Tytler, D., Kirkman, D., O'Meara, J. M., & Lubin, D. 2005, ApJ,
Thomas, R., Le Fèvre, O., Le Brun, V., et al. 2017, A&A, 597, A88
Tummuangpak, P., Bielby, R. M., Shanks, T., et al. 2014, MNRAS, 442, 2094
Turner, M. L., Schaye, J., Steidel, C. C., Rudie, G. C., & Strom, A. L. 2014,
   MNRAS, 445, 794
van de Voort, F. 2017, in Gas Accretion onto Galaxies, ed. A. Fox & R. Davé,
   Vol. 430 (Berlin: Springer), 301
Villarroel, B., & Korn, A. J. 2014, NatPh, 10, 417
White, M., Myers, A. D., Ross, N. P., et al. 2012, MNRAS, 424, 933
Wright, E. L., Eisenhardt, P. R. M., Mainzer, A. K., et al. 2010, AJ, 140,
  1868
York, D. G., Adelman, J., Anderson, J. E., Jr, et al. 2000, AJ, 120, 1579
Youles, S., Bautista, J. E., Font-Ribera, A., et al. 2022, MNRAS, 516, 421
Zakamska, N. L., Strauss, M. A., Krolik, J. H., et al. 2003, AJ, 126, 2125
Zhang, Y., Ouchi, M., Gebhardt, K., et al. 2021, ApJ, 922, 167
```